

One-shot free energy calculations for crystalline materials

Thesis for the Degree Master of Science

TOMMY ANDERSSON

Department of Applied Physics
CHALMERS UNIVERSITY OF TECHNOLOGY
Gothenburg, Sweden 2012

Abstract

Current methods for free energy calculations in materials science are either computationally expensive, as λ -integration, or based on the harmonic approximation and thus only applicable to materials with stable lattices. Thus, a computationally cheap yet highly accurate method with broad applicability is sought after.

The objective of this thesis is to establish a method for one-shot free energy calculations utilizing effective harmonic models, obtained by fitting forces from molecular dynamics simulations. This approach enables extraction of effective harmonic representations of fully anharmonic crystals at finite temperatures. In addition, residual corrections to the free energy are incorporated using free energy perturbation.

Three systems are considered, titanium, iron and a dimer. The dimer is studied to highlight general features of harmonic models, whereas iron is considered as a robust test system for verification during method development. Finally, titanium is used as an example for a system with a rich temperature-pressure phase diagram featuring several entropically stabilized phases. λ -integration and velocity auto-correlation functions serve as reference methods for comparison of the free energy and phonon properties, respectively.

Excellent agreement with reference methods is reported for phonon dispersion and free energy in iron. For titanium the approach successfully reproduces the temperature dependence of soft modes. The resulting free energies exhibit larger deviations from the reference data than in iron. An improvement in this work compared to a similar approach recently published is the reduction of the number of parameters enabled by using symmetry properties directly during force matching and the application of free energy perturbation.

The proposed model requires only one simulation whereas λ -integration requires typically on the order of ten simulations. Hence, the proposed method reduces the total simulation time with a factor of 10. The approach outlined in this thesis enables accurate free energy calculations for arbitrary crystalline materials at a greatly reduced cost. It is therefore ideally suited for simulations based on electronic structure methods such as density functional theory.

Acknowledgements

I would like to thank my supervisor Paul Erhart for guiding me throughout this project. Paul's enthusiasm and willingness to share knowledge, his patience and collaborative spirit have made the work with the project challenging, fun and exciting.

Further, I would also like to thank Anders Lindman for giving advice regarding stylistic aspects of the text in this report, as well as for accompanying me during lunches and coffee breaks.

Tommy Andersson, Göteborg 2012-06-11

List of abbreviations

<i>NPT</i>	Isobaric-isothermal ensemble
<i>NVE</i>	Microcanonical ensemble
<i>NVT</i>	Canonical ensemble
bcc	Body-centered cubic
DFT	Density functional theory
DOS	Density of states
EAM	Embedded atom method
EHM	Effective harmonic model
FEP	Free energy perturbation
FFT	Fast Fourier transform
HA	Harmonic approximation
MD	Molecular dynamics
MEAM	Modified embedded atom method
QHA	Quasi-harmonic approximation
SVD	Singular value decomposition
VAC	Velocity autocorrelation

Contents

1	Introduction	1
1.1	Background	1
1.2	Scope	2
2	Molecular dynamics simulations	5
2.1	Relation to experiments	5
2.2	Ensembles	6
2.3	Empirical potentials	6
3	Methods	9
3.1	λ -integration	9
3.2	Harmonic models	11
3.3	Free energy perturbation	15
3.4	Velocity autocorrelation	16
4	Dimer	17
5	Iron	21
5.1	Time step and thermal expansion	21
5.2	λ -integration	22
5.3	Effective harmonic models	24
5.4	Method comparison	30
6	Titanium	33
6.1	Martensitic transition	33
6.2	Effective harmonic models	36
6.3	λ -integration	40
6.4	Method comparison	42
6.5	Phase diagram	43

7	Discussion	47
7.1	Dimer	47
7.2	Iron	48
7.3	Titanium	49
8	Conclusions	53
	Bibliography	57

1

Introduction

The ability to predict and understand structural behavior of materials under pressure and temperature is of vital importance in both science and technology. Various industries, such as automotive as well as aero and space industry, are driven by light yet strong materials that can be used in frames and engines to obtain for example enhanced durability and lower fuel consumption. More recent applications of cutting edge materials science are biomedical implants and consumer products such as cameras and golf clubs [1].

Thermodynamics ascertains that the free energy is minimal in thermal equilibrium. Knowledge of the free energy landscape is therefore key for understanding materials properties and performance. While for many systems the free energy is well described within the harmonic approximation (HA), this approach fails for a considerable number of scientifically and technologically important materials that are strongly anharmonic or even mechanically unstable at zero temperature. The objective of the present thesis is to establish a method for obtaining free energies from one-shot molecular dynamics (MD) simulations that is applicable to arbitrary crystalline materials removing the constraints of the standard HA. This approach implicitly incorporates phonon-phonon interactions and represents an improvement compared to the HA for all crystalline systems.

1.1 Background

Density functional theory (DFT) enables accurate calculations of materials properties based on a quantum mechanical description of the electronic structure [2]. Combining DFT with MD simulations allows studying systems at finite temperature. DFT calculations, however, are still computationally very expensive and

therefore restricted to small systems and short time scales.

Empirical potentials consider interactions between atoms rather than electrons. They are therefore computationally far more efficient than DFT calculations but lack the accuracy and transferability of the latter.

Free energies can be calculated in a few different ways. The self-consistent *ab initio* lattice dynamics approach by Souvatzis *et al.* [3] incorporates effective temperature dependence of phonon frequencies via a finite displacement method. This method has been used for example to reproduce the experimental phonon dispersions of high temperature phases of group IV metals [4]. Recently Hellman *et al.* [5] proposed a method based on classical molecular dynamics simulations. In their work an effective harmonic representation of an anharmonic system is extracted by fitting the full force-constant matrix. They report excellent agreement with experimental phonon dispersions in lithium and zirconium, as well as good agreement with the experimental phase diagram of zirconium. Their approach requires fitting on the order of N^2 matrix elements, where N is the number of degrees of freedom in the *supercell* used in the simulations. It is furthermore noteworthy that the accuracy of the free energies in Ref. [5] has been neither assessed in terms of size convergence nor compared to a reference method such as λ -integration [6].

1.2 Scope

The objective of this project has been to develop a method for free energy calculations suitable for anharmonic crystals. Similarly to the work by Hellman *et al.* the spirit in this work has been to fit temperature dependent harmonic models for anharmonic systems. The approach described in this thesis, however, requires fitting only on the order of $10 \times n$ parameters, where n is the number of symmetry inequivalent atoms in the primitive unit cell. A major focus has been to determine the accuracy of the free energy obtained in this fashion by comparison with λ -integration. In addition free energy perturbation corrections [7] have been applied.

There are several ways to fit harmonic models, which means there is not a *single optimal* harmonic fit for a given system. The *derivative based* quasi-harmonic approximation (QHA) is a static lattice method that neglects anharmonicity, where temperature dependence is approximately incorporated through temperature dependent volumes. Alternatively, harmonic models can be constructed by considering correlations between displacements of different atoms in MD simulations [8]. This approach incorporates finite temperature effects and is expected to provide better estimates of the free energy.

Two new methods are evaluated in this thesis. The first employs singular

value decomposition (SVD), whereas the second is based on fitting symmetry reduced force constants. These methods are compared with reference methods. λ -integration is used as reference method for free energy calculations, whereas phonon properties are compared with results from velocity autocorrelation (VAC) functions. Since λ -integration requires a series of simulations while the new method requires only a single simulation the latter is referred to as a *one-shot* approach. This approach explicitly incorporates finite temperature effects, and thus yields *effective* harmonic models (EHMs).

Three different systems have been studied. First a system with only two atoms, a dimer, was studied. The atoms interact through a Morse potential, and the system behaves as a strongly anharmonic oscillator. This textbook example is used to highlight the advantages and limitations of harmonic representations. The second system that was studied was a body-centered cubic (bcc) iron crystal. This serves as a robust test system for validation and benchmarking of the new methods. The third and final material that has been studied is titanium. Since the high temperature bcc phase is dynamically unstable at zero K and is thermally stabilized by phonon-phonon coupling the QHA cannot be applied [9, 10]. The first goal of this work has been to determine the accuracy that can be achieved using EHMs. The second goal has been to evaluate the computational cost by comparing computational efficiency of the EHM approach with conventional λ -integration. The model systems were simulated using empirical potentials in order to obtain results that are numerically fully converged. Eventually the utility of the approach outlined in this thesis, however, lies in its applicability to electron structure calculations as DFT.

The report is organized as follows. In chapter 2 the basics of the simulation technique are presented. General aspects of molecular dynamics simulations are discussed first, followed by a description of different ensembles and the empirical potentials used in this work. In chapter 3 details of the methods for free energy calculations are presented. First λ -integration is described, followed by the harmonic approximation and the EHM scheme proposed in this work. Free energy perturbation (FEP) is introduced as a means to incorporate residual anharmonic corrections to the free energy. Finally the VAC approach to obtain phonon properties is presented. In chapters 4, 5 and 6 method evaluation, free energy calculations and results for dimer, iron and titanium are presented. In chapter 7 results from chapter 4, 5 and 6 are discussed. Conclusions are summarized in chapter 8.

2

Molecular dynamics simulations

Molecular dynamics (MD) is a classical simulation technique for many-body systems such as gases, liquids and solids. Classical means in this context solving the equations of motions from classical mechanics, which implies that quantum mechanical effects are ignored. In this work the open-source MD code LAMMPS has been used [11].

2.1 Relation to experiments

Performing MD simulations very much resembles experiments. First chemical composition and structure of the system have to be specified, such as number of atoms, atom types, lattice structure, boundary conditions and interaction potential. Subsequently thermodynamic boundary conditions have to be chosen, corresponding to proper thermodynamical ensembles, e.g. canonical (NVT), microcanonical (NVE), or isobaric-isothermal (NPT).

The simulation is started with equilibrating the system under the desired conditions, i.e. a specific pressure and/or temperature. Subsequently equilibrium quantities such as potential- and kinetic energy or particle position and velocity can be calculated. Observables in classical thermodynamic correspond to ensemble averages in statistical mechanics. To obtain thermodynamic quantities from MD simulations the system is assumed to be ergodic, which enables replacing ensemble averages with time averages. As in a real experiment there are fluctuations and noise of measured quantities. Extending the length of the simulation reduces uncertainty in the estimated quantities.

2.2 Ensembles

The natural way to perform MD simulations is in the microcanonical NVE -ensemble, that is, to let the system evolve according to the classical equations of motions without any coupling to external baths. More commonly one is however interested in the canonical ensemble which represents equilibrium with respect to an external heat bath. In practice this can be accomplished by modifying the equations of motion by introducing an artificial parameter that couples to the particle velocities. By introducing this parameter the temperature can be controlled and time averages from simulations will equal canonical ensemble averages. For further details about temperature control in the extended-Lagrangian formulation see pp. 148 in Ref. [12]. Similarly to adding temperature control one can implement pressure control. The pressure control changes the volume of the system to reach a target pressure and the resulting ensemble is known as the isothermal-isobaric NPT ensemble.

In the present work simulations were carried out in NVE , NVT and NPT ensembles. Nosé-Hoover thermostat and barostat have been used for temperature and pressure control [13–16].

2.3 Empirical potentials

The iron system presented in chapter 5 has been modeled with an embedded atom method (EAM) potential [17]. In the EAM formalism [18–20] the potential energy of atom i is given by

$$E_i = F_a \left[\sum_{j \neq i} \rho_b(r_{ij}) \right] + \frac{1}{2} \sum_{j \neq i} \phi_{ab}(r_{ij}),$$

where r_{ij} is the distance between atoms i and j , and ϕ_{ab} is a pairwise potential with subscripts denoting atom types, ρ_b is the electron density of atom of type b . Finally, F_a is an embedding potential representing the energy of placing an atom of type a into the electron cloud. Summations are performed only over atoms that are within a potential specific cut-off distance. Note that each atom contributes with a spherical symmetric electron density.

The titanium system presented in chapter 6 has been modeled with a modified embedded atom method (MEAM) potential [21, 22]. In the MEAM formalism the potential energy of atom i is given by

$$E_i = F_a(\tilde{\rho}_i) + \frac{1}{2} \sum_{j \neq i} \phi_{ab}(r_{ij}),$$

which takes bond directionality into account in the calculation of the electron density $\tilde{\rho}_i$. While this extends the flexibility and application range of the potential it also renders MEAM potentials computationally more expensive than EAM potentials.

3

Methods

In this chapter the computational methods used in this work are described in more detail. λ -integration, which is the reference method for the free energy calculations, is outlined in section 3.1. In section 3.2 harmonic models are discussed. After introducing the harmonic approximation, two schemes for fitting *effective* harmonic models are described. The free energy perturbation correction allows taking into account anharmonic contribution beyond effective harmonic models is presented in section 3.3. Finally the velocity autocorrelation function approach to obtain phonon properties is presented in 3.4.

3.1 λ -integration

The coupling parameter method, also known as λ -integration, was proposed by Kirkwood in 1935 [23], and implemented in the context of computer simulations of particle systems by Frenkel and Ladd [6]. It is a general method that enables calculation of free energies by doing thermodynamic integration. An integrable path that links the target system S_1 to a reference system S_0 is constructed through a parameterized potential $U(\lambda)$. The main goal in this section is to show that the free energy can be obtained by integration along this path.

The reference system should be chosen such that its free energy is known and such that it can be switched smoothly into the target system. For the solid state an appropriate reference system is the Einstein crystal, which is a system of N independent identical harmonic oscillators. The internal energy U_0 of the Einstein

crystal is given by the displacements from the ideal lattice positions

$$U_0 = \alpha/2 \sum_{i=1}^N (\mathbf{r}_i - \mathbf{r}_{0,i})^2,$$

where α denotes the spring constant of the oscillators. Taking finite size corrections into account the free energy of the Einstein crystal takes the form

$$\frac{F_0}{Nk_B T} = -\frac{3}{2} \ln \left(\frac{k_B^2 T^2 m}{\hbar^2 \alpha} \right) - \frac{3}{2N} \ln \left(\frac{\alpha}{2\pi k_B T} \right) - \frac{1}{N} \ln \left(\frac{N}{V} \right) - \frac{3}{2N} \ln(N),$$

where m is the mass of the oscillating particle, k_B is Boltzmann's constant, \hbar is Planck's constant, T is the temperature and V is the volume [24]. To construct the integrable path one now specifies the parameterized potential as a linear combination of the target potential U_1 and the reference potential U_0 as follows

$$U(\lambda) = U_0 + \lambda(U_1 - U_0).$$

For $\lambda = 0$ the parameterized potential describes the Einstein crystal whereas for $\lambda = 1$ it describes the target system, and by letting $\lambda : 0 \rightarrow 1$ one can smoothly switch between the two systems. The configurational partition function \mathcal{Z}_λ for a canonical ensemble (NVT ensemble), i.e. when the number of particles is fixed and volume and temperature are constant, is given by

$$\mathcal{Z}_\lambda = \int \exp(-U(\lambda)/k_B T) d\mathbf{x},$$

where the integral extends over the entire configuration space. The partition function is linked to the free energy via

$$F_\lambda = -k_B T \ln \mathcal{Z}_\lambda. \quad (3.1)$$

By taking the derivative of eq. (3.1) with respect to λ and integrating from 0 to 1 one arrives at the following result

$$F_1 = F_0 + \int_0^1 d\lambda \left\langle \frac{\partial U(\lambda)}{\partial \lambda} \right\rangle_\lambda = F_0 + \int_0^1 d\lambda \langle U_1 - U_0 \rangle_\lambda, \quad (3.2)$$

which expresses that by sampling $\langle U_1 - U_0 \rangle_\lambda$ for configurations generated by $U(\lambda)$ where $\lambda : 0 \rightarrow 1$ the free energy of the target system F_1 can be calculated. One has to ensure that the integration path is chosen such that the integrand $\langle U_1 - U_0 \rangle_\lambda$ is continuous. Integrating over a first order phase transition is therefore problematic [12].

3.2 Harmonic models

At low temperatures T many solid materials behave as if the interatomic potential would be of purely harmonic character. This correlates with the fact that the atomic mean square displacement $\langle u^2 \rangle$ approaches zero at low T . Mathematically speaking a series expansion of the interatomic potential around the static lattice shows that the leading contribution at low T is quadratic and contribution from higher order terms are negligible due to small displacements u_i at low T [25].

In the harmonic approximation one tries to describe the behavior of the real system using only the lowest order non-vanishing terms in the expansion. The potential energy of the system is then given by

$$\phi(\mathbf{r}) = 1/2 \sum_{ij\alpha\beta} \phi_{ij}^{\alpha\beta} u_i^\alpha u_j^\beta, \quad (3.3)$$

where the indices denote atoms i and j respectively, while α and β denote cartesian directions. Each atom is coupled to every other atom with a spring which means that the forces are linear in the displacements. The elements of the $3N \times 3N$ force constant matrix are denoted by $\phi_{ij}^{\alpha\beta}$, where N is the number of atoms, and u_i^α denotes the displacement of atom i from its ideal position along direction α . The matrix elements $\phi_{ij}^{\alpha\beta}$ are the parameters of this model, and can be obtained in different ways.

From the force constant matrix the dynamical matrix can be determined. To express the dynamical matrix the atom indices $i(j)$ are unfolded into collective indices $l(l')$, $k(k')$ which label unit cell and atom within each unit cell, respectively. In this notation the associations are as follows $i \leftrightarrow lk$ and $j \leftrightarrow l'k'$ and the dynamical matrix reads

$$\mathbf{D}_{\alpha\beta}^{kk'}(\mathbf{q}) = \frac{1}{\sqrt{m_k m_{k'}}} \sum_l \phi_{ij}^{\alpha\beta} \exp [i\mathbf{q} \cdot (\mathbf{r}_{j,0} - \mathbf{r}_{i,0})]. \quad (3.4)$$

Where $\mathbf{D}_{\alpha\beta}^{kk'}(\mathbf{q})$ is an $3n \times 3n$ matrix, n is the number of atoms in the unit cell, and $\mathbf{r}_{i,0}$ denotes the average position of atom k in unit cell l . Using the conventional ansatz, in the spirit of eq. (3.13), displacements can be expressed as a superposition of phonon modes. Substituting this ansatz into the equations of motion and requiring non-trivial solutions leads to the following condition

$$|\mathbf{D}_{\alpha\beta}^{kk'}(\mathbf{q}) - \omega^2(\mathbf{q})\mathbf{I}| = 0. \quad (3.5)$$

Solving this equation gives the phonon dispersion [26]. Note that each wave vector \mathbf{q} is associated with $3n$ eigenvalues and that \mathbf{I} is a $3n \times 3n$ identity matrix. Since the dynamical matrix is Hermitian the eigenvalues $\omega^2(\mathbf{q})$ are real. The square root of

the eigenvalues are the phonon frequencies $\omega(\mathbf{q})$. By diagonalizing the dynamical matrices one can thus obtain the phonon spectrum. For a more elaborate discussion of dynamical matrices see Ref. [27].

From the phonon dispersion one can compute the phonon density of states and harmonic free energy to study dynamical properties, structure and stability aspects. An expression for the classical harmonic free energy F_H can be obtained the following way. First the potential energy is expressed in a quadratic form

$$\phi(\mathbf{r}) = \mathbf{u}^T \mathbf{Q} \mathbf{u}, \quad (3.6)$$

which is a reformulation of eq. (3.3), where $\mathbf{Q} \in \mathbb{R}^{3N \times 3N}$ is the force constant matrix and $\mathbf{u} \in \mathbb{R}^{3N}$ are the atomic displacements. The corresponding configurational partition function is

$$\mathcal{Z} = \int \exp(-\mathbf{u}^T \mathbf{Q} \mathbf{u} / k_B T) d\mathbf{u} = \int \exp(-\mathbf{u}^T \mathbf{K}^T \mathbf{D} \mathbf{K} \mathbf{u} / k_B T) d\mathbf{u}. \quad (3.7)$$

where the force constant matrix has been diagonalized $\mathbf{Q} = \mathbf{K}^T \mathbf{D} \mathbf{K}$. The configurational partition function can then be written

$$\mathcal{Z} = \prod_{i=1}^{3N} \int_{-\infty}^{\infty} \exp(-\nu_i^2 \omega_i^2 / k_B T) d\omega_i, \quad (3.8)$$

which is a product of gaussian integrals. The ν_i 's are the square roots of the diagonal elements $\sqrt{\mathbf{D}_{ii}}$ and carry the information about the phonon spectrum. Insertion of the partition function in eq. (3.1) yields the vibrational free energy

$$F_{vib} = -k_B T \left[\frac{3}{2} \ln \left(\frac{2\pi}{k_B T} \right) - \frac{1}{N} \sum_{i=1}^{3N} \ln \nu_i \right]. \quad (3.9)$$

Apart from a constant shift due to the static lattice energy this is the expression that has been used for the harmonic free energies in chapter 5 and 6. In the next sections distinct schemes for determining the parameters in a harmonic model are presented. The elements of the force constant matrix $\phi_{ij}^{\alpha\beta}$ are the parameters in section 3.2.1 and 3.2.2, whereas the phonon spectrum ν_i is fitted directly in section 3.2.3.

3.2.1 Derivative based approach

The most common approach for calculating free energies of crystalline solids invokes the so-called quasi-harmonic approximation (QHA). In this scheme the force constant matrix is obtained by explicitly computing the second derivative of the

potential energy for the static lattice (corresponding to zero K). In addition, a volume range is scanned to find the trace in the temperature-volume plane that minimizes the free energy. In this fashion the leading contribution to thermal expansion included. This is not the case in the harmonic approximation (HA), where the volume is fixed.

3.2.2 Effective harmonic models

A substantial number of materials of scientific and/or technological interest are mechanically unstable at zero K. This implies that eigenvalues of the dynamical matrices are negative yielding imaginary frequencies. As a result the QHA is strictly not applicable. Instead, an approach where the force constant matrix is fitted to forces from MD simulations can be employed. This yields a harmonic model that embodies an effective representation of the fully anharmonic system.

As pointed out previously the force constant matrix scales quadratically N^2 with the number of atoms in the systems, but the matrix elements are not all independent. From the given crystal structure the number of independent elements is reduced by symmetry. Furthermore, a cut-off radius, which is an upper limit to the length scale at which interactions are important, can usually be established. In our case this simply boils down to the number of neighbor shells that are included. In this picture the potential energy in the effective harmonic model (EHM) can be expressed

$$\phi(\mathbf{r}) = 1/2 \sum_{ij\alpha\beta} \kappa_{ij}^{\alpha\beta} u_i^\alpha u_j^\beta r_{ij}^\alpha r_{ij}^\beta, \quad (3.10)$$

where $\kappa_{ij}^{\alpha\beta}$ is an element of a reduced force constant matrix, and r_{ij}^α is the α component of the normalized bond vector connecting atoms i and j . The summation over ij is restricted to pairs within the cut-off range. The reduced force constant matrix is essentially a sub-matrix of the full force constant matrix. The product of the bond vector components $r_{ij}^\alpha r_{ij}^\beta$ corresponds to a rotation of the matrix with respect to the bond. For bcc crystals the reduced force constant matrix $\kappa_{(1)}$ representing the nearest neighbor interaction reads

$$\kappa_{(1)} = \begin{pmatrix} a_1 & b_1 & b_1 \\ b_1 & a_1 & b_1 \\ b_1 & b_1 & a_1 \end{pmatrix}.$$

Next-nearest neighbors are located along $\langle 100 \rangle$, which implies that off-diagonal

elements will be zero, since $r_{ij}^\alpha r_{ij}^\beta = \delta_{\alpha\beta}$. Thus, $\kappa_{(2)}$ is diagonal, and reads

$$\kappa_{(2)} = \begin{pmatrix} a_2 & 0 & 0 \\ 0 & a_2 & 0 \\ 0 & 0 & a_2 \end{pmatrix}.$$

The reduction of the number of independent elements is deduced from the lattice symmetry. Similarly $\kappa_{(3)}, \kappa_{(4)}, \dots$ will be 3×3 matrices, for bcc systems. For other crystal structures the reduced force constant matrix grows with the number of atoms in the primitive cell. It is computationally more efficient to use the symmetry properties directly in the fitting process, as described here, rather than fitting the full force constant matrix as in Ref. [5], where symmetrization is carried out at a later stage.

Only the structure of the reduced force constant matrices has been discussed so far but not the actual fitting procedure. The force constants are optimized in a least square sense where the residual

$$\chi^2 = \frac{1}{3CN} \sum_{i=1}^C \sum_{j=1}^N \sum_{\alpha}^{x,y,z} \left(f_{ij\alpha}^{(p)} - f_{ij\alpha}^{(t)} \right)^2 \quad (3.11)$$

is minimized. Here C is the number of configurations, N is the number of atoms, α is the cartesian direction, $f_{ij\alpha}^{(p)}$ is the predicted force and $f_{ij\alpha}^{(t)}$ is the target force. Minimization is performed using the conjugate gradient method.

3.2.3 Singular value decomposition

In this work yet another approach to constructing EHM's using singular value decomposition (SVD) has been explored. Within the harmonic approximation displacements of atoms from equilibrium positions $\mathbf{u}(t) = \mathbf{r}(t) - \mathbf{r}_0$ can be expressed as a superposition of normal modes

$$\mathbf{u}(t) = \sum_k a_k \exp(i\omega_k t) \xi_k \quad (3.12)$$

where $\mathbf{u}(t) \in \mathbb{R}^{3N}$ refer to the displacement from the ideal positions at time t . Furthermore, a_k , ω_k and ξ_k denote amplitude, frequency and polarization vector of phonon mode k . For our purposes it is more convenient to rewrite eq. (3.12) in component form

$$u_i(t) = \sum_k a_k \exp(i\omega_k t) \xi_{ik}. \quad (3.13)$$

Discretizing in time by replacing $t \rightarrow j\Delta t$ eq. (3.12) can be formulated in index notation as

$$u_{ij} = \sum_k a_k w_{kj} \xi_{ik}, \quad (3.14)$$

where $w_{kj} = \exp(i\omega_k j\Delta t)$. Now consider the SVD of a $n \times m$ matrix \mathbf{M} in index notation

$$M_{ij} = \sum_{kl} U_{ik} S_{kl} V_{lj}, \quad (3.15)$$

here $\mathbf{U} \in \mathbb{R}^{n \times n}$, $\mathbf{S} \in \mathbb{R}^{n \times m}$ and $\mathbf{V} \in \mathbb{R}^{m \times m}$ where \mathbf{U} and \mathbf{V} are Hermitian. In addition \mathbf{S} is diagonal which leads to

$$M_{ij} = \sum_k U_{ik} S_k V_{kj}. \quad (3.16)$$

By comparison with eq. (3.14) one immediately obtains the following relations

$$\begin{aligned} M_{ij} &= u_{ij}, \\ U_{ik} &= \xi_{ik}, \\ S_k &= a_k, \\ V_{kj} &= w_{kj} = \exp(i\omega_k t), \end{aligned}$$

where w_{kj} contains information about the phonon frequencies ω_k . This suggests that the harmonic phonons can be directly obtained from the decomposition of the displacement matrix without explicitly fitting force constants. In addition, phonon life times can be extracted from the broadening of the spectrum. One difference between this approach and the method described in the previous section is that here we rely on using strongly correlated configurations, that is, the time window between snapshots must be small compared to the time scale of the dynamics. For the previous approach it is rather the opposite as one requires independent decorrelated configurations.

3.3 Free energy perturbation

Describing an anharmonic system with a harmonic model may lead to a systematic deviation of the harmonic free energy from the true free energy. The free energy perturbation (FEP) formula of Zwanzig [7] can be used to estimate this deviation. Its derivation is straightforward as shown in the following. In statistical mechanics the partition function \mathcal{Z} is given by

$$\mathcal{Z} = \int dx d\mathbf{p} \exp(-\beta\mathcal{H}),$$

where $\mathcal{H} = T + U$ is the Hamiltonian of the system. Assuming the potential energy is velocity independent the ratio of the partition function of the fully anharmonic system \mathcal{Z}_1 and the harmonic partition function \mathcal{Z}_0 can be written as

$$\frac{\mathcal{Z}_0}{\mathcal{Z}_1} = \frac{\int d\mathbf{x}d\mathbf{p}e^{-\beta(T_0+U_0)}}{\int d\mathbf{x}d\mathbf{p}e^{-\beta(T_1+U_1)}} = \frac{\int d\mathbf{x}e^{-\beta U_1}e^{-\beta(U_0-U_1)}}{\int d\mathbf{x}e^{-\beta U_1}} = \langle e^{-\beta(U_0-U_1)} \rangle_1,$$

where T_i, U_i are kinetic and potential energy respectively. The brackets $\langle \cdot \rangle_1$ denote the ensemble average and the subscript 1 indicates that the average is generated by sampling the fully anharmonic system. Using eq. (3.1) the free energy difference $\Delta F = F_0 - F_1$ can be written

$$\Delta F = -\frac{1}{\beta} \ln \left(\langle e^{-\beta(U_0-U_1)} \rangle_1 \right),$$

which expresses that calculating the potential energy difference $U_0 - U_1$, from configurations generated with the full potential, a correction to the harmonic free energy can be obtained. The free energy of the fully anharmonic system is then given by

$$F_1 = F_0 + \frac{1}{\beta} \ln \left(\langle e^{-\beta(U_0-U_1)} \rangle_1 \right), \quad (3.17)$$

which is known as Zwanzig's equation.

3.4 Velocity autocorrelation

Fourier transformation of the velocity autocorrelation (VAC) function is a method for determining phonon dispersions at elevated temperatures [28, 29]. This approach is prone to finite size effects, and thus requires large systems. The normalized VAC function is defined as

$$C_v(\tau) = \frac{\langle v_n(\tau)v_0(0) \rangle}{\langle v_n(0)v_0(0) \rangle}, \quad (3.18)$$

where the expectation value is given by

$$\langle v_n(\tau)v_0(0) \rangle = \frac{1}{\tilde{\tau}3N} \sum_t^{\tilde{\tau}} \sum_i^{3N} v_i(t+\tau)v_i(t), \quad (3.19)$$

here the summation ranges over all snapshots in time from 0 to $\tilde{\tau}$, and over the $3N$ velocity components. The Fourier transform of the VAC gives the phonon spectral density, which in turn is proportional to the phonon density of states (DOS). Mathematically this is expressed as

$$\text{DOS}(\omega) \propto \int_{-\infty}^{\infty} d\tau e^{i\omega\tau} C_v(\tau). \quad (3.20)$$

This expression has been used to calculate DOS for the iron system in chapter 5.

4

Dimer

A dimer is a system with only two atoms. Due to its simplicity it is well suited as a starting point for studying the validity of the harmonic approximation and the importance of anharmonic effects. The aim is to illustrate general features and limitations of harmonic representations.

Specifically, two identical particles with a mass of 50 atomic mass units were considered. The interaction between the particles was modeled using a Morse potential,

$$U = D_0 [e^{-2\alpha(r-r_0)} - 2e^{-\alpha(r-r_0)}], \quad (4.1)$$

where r , $r_0 = 1.5 \text{ \AA}$, are particle separation and equilibrium separation, $D_0 = 3 \text{ eV}$ and $\alpha = 2 \text{ \AA}^{-1}$, which sets energy scale and curvature, respectively. The particles were initiated with velocities in opposite directions and the system evolved under the influence of the potential. The velocity range from 0.01 \AA/ps to 1.4 \AA/ps was considered. At the lower end of this range the system is described very well within the harmonic approximation while at the higher end anharmonicity is strong.

Figure 4.1 shows the Morse potential, the trajectory of the dimer and illustrates the harmonic fit to the forces in the simulation. At a velocity of 0.1 \AA/ps one observes very good agreement between harmonic fit and full potential. Since the deviation from the equilibrium bond length is small the harmonic approximation describes the system well. As the velocity is increased, the discrepancy between harmonic fit and full potential increases. At a larger velocity of 1.0 \AA/ps the effective harmonic potential is much softer and the mismatch with the full potential is very apparent.

It is instructive to compare the characteristic oscillation frequency of the dimer with the frequency deduced from the harmonic fit. The characteristic oscillation frequency, defined as the main peak in the frequency spectra, is obtained by

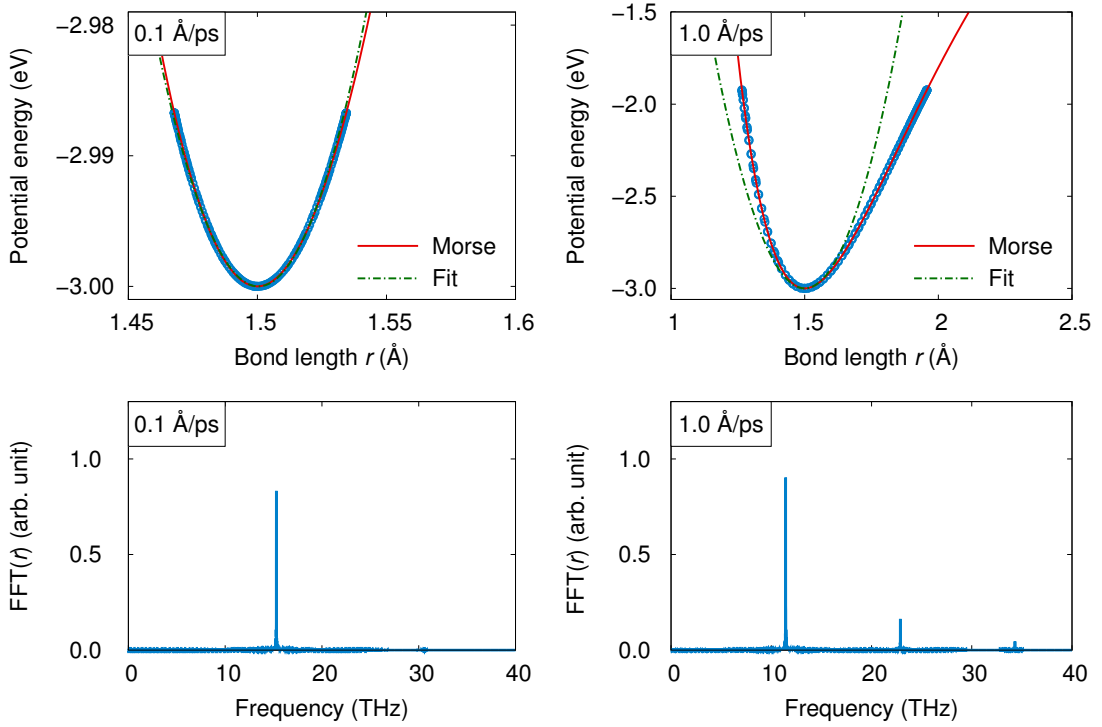


Figure 4.1: Morse potential and harmonic fit are plotted for 0.1 and 1.0 Å/ps in the upper panels. The harmonic fit is obtained by fitting one force constant to the forces in the simulation. The characteristic oscillation frequency obtained by Fourier transformation of the time evolution of bond length is shown in the lower panels. Higher harmonics are observed at 1.0 Å/ps.

Fourier transformation of the time evolution of the bond length, see Figure 4.1. One frequency component is dominating at 0.1 Å/ps whereas higher harmonics are observed as a result of anharmonicity at 1.0 Å/ps. This frequency is to be used as reference and compared with the frequency deduced from fitting the force constant. Note that there is only one force constant for the harmonic dimer and the corresponding frequency is given by $\omega = \sqrt{k/\mu}$ where μ is the reduced mass of the system.

A comparison between characteristic frequencies and harmonic frequencies is shown in Figure 4.2. The overall agreement is good, and at the lower end of the range excellent agreement is observed. The discrepancy increases with velocity which is due to the fact that increased velocity leads to significant probing of the anharmonic parts of the potential. As more and more anharmonic parts of the configuration space are explored the harmonic approximation should be used with caution.

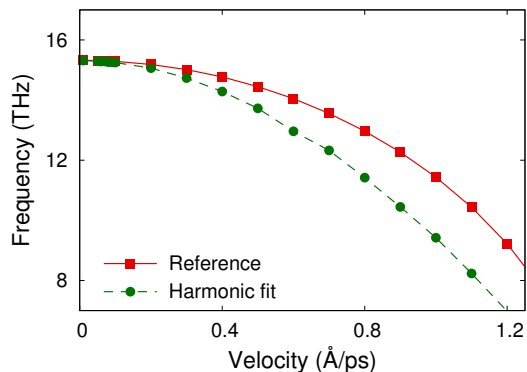


Figure 4.2: Characteristic oscillation frequency of the dimer. The reference is obtained by Fourier transformation of the time evolution of bond length. The harmonic fit is obtained by fitting one force constant to the forces in the simulation.

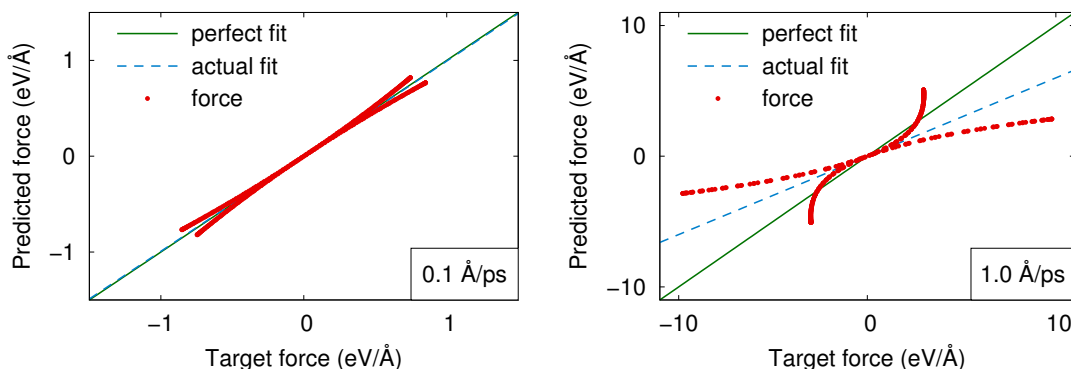


Figure 4.3: Scatterplot for velocities 0.1, 1.0 Å/ps respectively. The effect of anharmonicity increases with velocity which is seen in the increased deviation from a perfect fit and the increased asymmetry.

To further discuss the limitations of harmonic representations we consider a scatter plot where predicted forces are compared with target forces, as shown in Figure 4.3. For a model that perfectly fits the target forces all points in the scatter plot would fall onto a line through the origin with slope one. One observes that for increasing initial velocity the discrepancy between predicted forces and target forces increases, in particular when the absolute value of the force is large.

The slope of the fit is less than one since minimization of the residual, see eq. (3.11), yields predicted forces that on average underestimate the target forces. This underestimation is systematic and hence represents a bias rather than a statistical uncertainty.

In the HA, the oscillation frequency of the dimer would be independent of velocity. Note that velocity plays the role of temperature in this context. In contrast to the HA, an EHM incorporates thermal motion which enables it to follow the reference frequency. The conclusion is that EHMs are performing well, but discrepancy between harmonic oscillation frequency and reference oscillation frequency is increasing with temperature. This discrepancy originates from a bias, and it is expected that it can be accounted for when it comes to free energies by using FEP, see section 3.3. This correction is discussed in the subsequent chapters about iron and titanium.

5

Iron

The motivation for studying the iron system, which is stable from zero K up to the melting point, is to verify and benchmark the methods described in chapter 3. The first aspects that are discussed in this chapter are the integration time step, which is a simulation setting, and thermal expansion, which is a calibration. Simulations and calculations related to λ -integration and harmonic models are presented in section 5.2 and 5.3, respectively. Results from the SVD approach are discussed in section 5.3.1, and the EHMs obtained from fitting the force constant matrix are presented in section 5.3.2. The chapter is concluded with a comparison and discussion of the calculated free energies.

5.1 Time step and thermal expansion

The integration time step must be chosen small enough to ensure energy conservation and avoid large discretization errors. At the same time it should be chosen as large as possible to use computational resources efficiently. Microcanonical simulations were carried out at 1200 K and the total energy was monitored. The time-evolution of the total energy is presented in Figure 5.1(a), where the 8 fs time step violates energy conservation. Furthermore, the 4 fs time step gives rise to small oscillations in total energy. A time step of 2 fs has therefore been concluded to be the optimum choice, balancing energy conservation and computational efficiency.

Thermal expansion in bcc iron has been studied by *NPT* simulations. In Figure 5.1(b) the resulting lattice parameters from 300 K to 1000 K at 0 GPa are presented. These lattice parameters have been used in *NVT* and *NVE* simulations presented later in this chapter. The corresponding volume expansion from 300 K to 1000 K is 2.5%. Even though this is a small expansion it is important to point

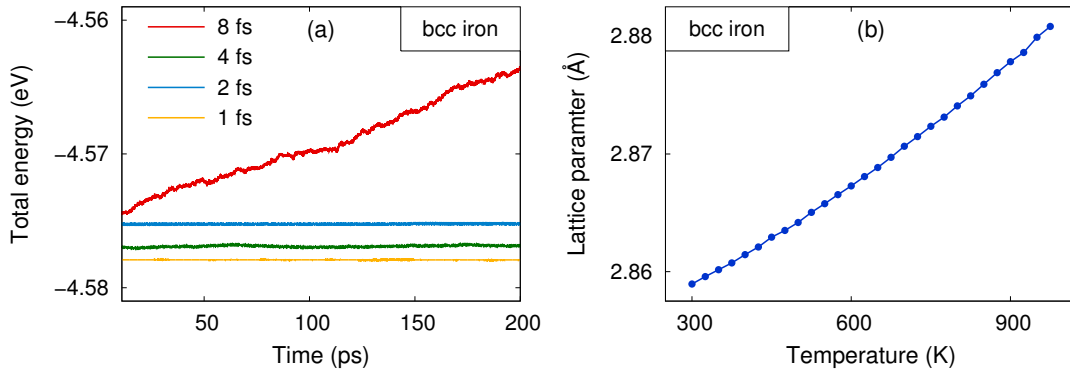


Figure 5.1: (a) Test of energy conservation where integration time-steps 1 fs, 2 fs, 4 fs and 8 fs are shown. (b) Temperature dependence of lattice parameter in BCC-iron at 0 GPa.

out that the measured pressure in NVT or NVE ensemble simulations is very sensitive with respect to changes in the lattice parameter.

5.2 λ -integration

The starting point for the λ -integration was to choose spring constant k for the Einstein crystal as well as to choose density of λ -values, where the spring constant should be chosen so that the Einstein crystal resembles the real system. The optimum value of the spring constant has been determined to $k = 7 \text{ eV}/\text{\AA}^2$ at 500 K from calculations of mean square displacement $\langle \Delta r^2 \rangle_\lambda$ and potential energy difference $\langle U_1 - U_0 \rangle_\lambda$. The corresponding plots of $\langle U_1 - U_0 \rangle_\lambda$ and $\langle \Delta r^2 \rangle_\lambda$ are shown in Figure 5.2.

An Einstein crystal is a non-interacting system. Due to lack of interactions a divergence of $\langle U_1 - U_0 \rangle_\lambda$ for small values of λ appears, see Figure 5.2. This originates from configurations with overlapping particles generated by sampling with λ close to zero. Those configurations will be very high in energy for the target system since it is strongly repulsive at short distances. This divergence is prominent for $k \leq 5 \text{ eV}/\text{\AA}^2$ at 500 K, and is even more pronounced as temperature is increased. To avoid the divergence a larger value of the spring constant $k = 20 \text{ eV}/\text{\AA}^2$ has been chosen. When choosing a stiff spring the potential energy difference falls off rapidly for λ close to one. At first this seems as if one divergence is replaced by another sharp fall off, but the latter is easier to handle. The density of λ has been chosen so that $\Delta\lambda = 0.05$. This choice is dense enough to enable an accurate fit of $\langle U_1 - U_0 \rangle_\lambda$ and it is also reasonable when considering use of computational resources.

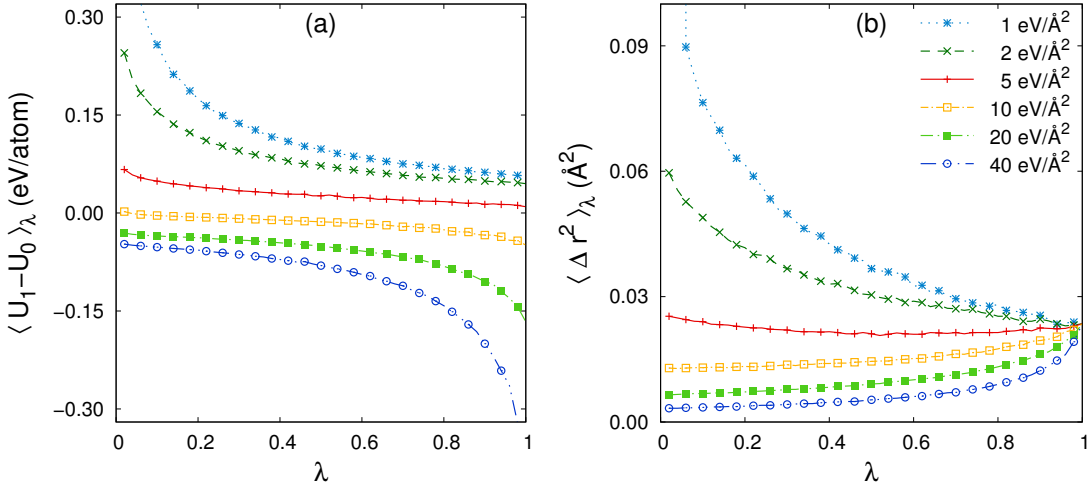


Figure 5.2: Spring constant value from $k = 1 \text{ eV/\AA}^2$ to $k = 40 \text{ eV/\AA}^2$, the temperature is 500 K. **(a)** The potential energy difference $\langle U_1 - U_0 \rangle_\lambda$ between the EAM iron potential and the Einstein crystal. **(b)** The mean square displacement $\langle \Delta r^2 \rangle_\lambda$.

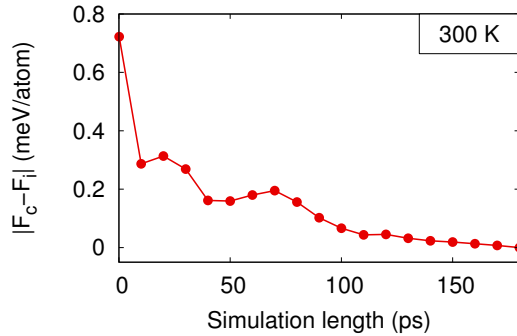


Figure 5.3: Convergence of the free energy from λ -integration at 300K for bcc iron.

To find a suitable simulation length the convergence of the free energy has been considered. In Figure 5.3 the difference $|F_c - F_i|$ is shown, where F_c is the converged value of the free energy, and F_i is the free energy obtained by using only a fraction of the time steps. The simulation is in total 200 ps long with a 20 ps initial equilibration, and a time step of 2 fs, and a temperature of 300 K. For an overview of the settings in the simulations see Table 5.1. Clearly the deviation is smaller than 0.1 meV/atom after 90 ps which indeed is promising. To accurately map out phase diagrams, which will be discussed for titanium in the next chapter, the uncertainty should be smaller than 1 meV/atom. The free energy using λ -integration is compared with the harmonic free energy from EHMs

in section 5.4.

Table 5.1: These settings were used for the NVT runs.

Time step (fs)	2
Simulation length (ps)	200
Equilibration time (ps)	20
System size (atoms)	250

5.3 Effective harmonic models

Two effective harmonic representations have been implemented and tested, namely the SVD approach and the effective harmonic model. In this section tests, verifications and results for these methods are presented.

5.3.1 Singular value decomposition

MD simulations were performed in the *NVE* ensemble. This is particularly important since the SVD approach relies on trajectories unperturbed by e.g., thermostating and/or barostating. A supercell with 250 atoms was used.

The SVD approach expresses atomic displacements as superpositions of harmonic phonon modes, see eq. (3.12). In this picture the term w_{kj} contains information about mode frequencies, see eq. (3.14). Two phonon modes, denoted mode 1 and mode 2 respectively, from a 300 K simulation are presented in Figure 5.4. This figure shows the time evolution of w_{kj} which is expected to oscillate harmonically in time, as well as the Fourier transform $\text{fft}(w_{kj})$ which is expected to have a sharp peak. The result for mode 1 is promising, it oscillates harmonically with only small modulations of the amplitude, and the corresponding Fourier transformation yields a sharp peak in the frequency spectrum. The results for mode 2, however, are less encouraging. Contrary to the results for mode 1, mode 2 is not oscillating harmonically, but exhibits damping as well as interfering frequencies, see Figure 5.4. Analysis of other modes shows that SVD generates frequency spectra without well-defined peaks. It was therefore concluded to abandon the SVD approach as it is unable to reliably separate all harmonic modes as required for calculating the harmonic free energy.

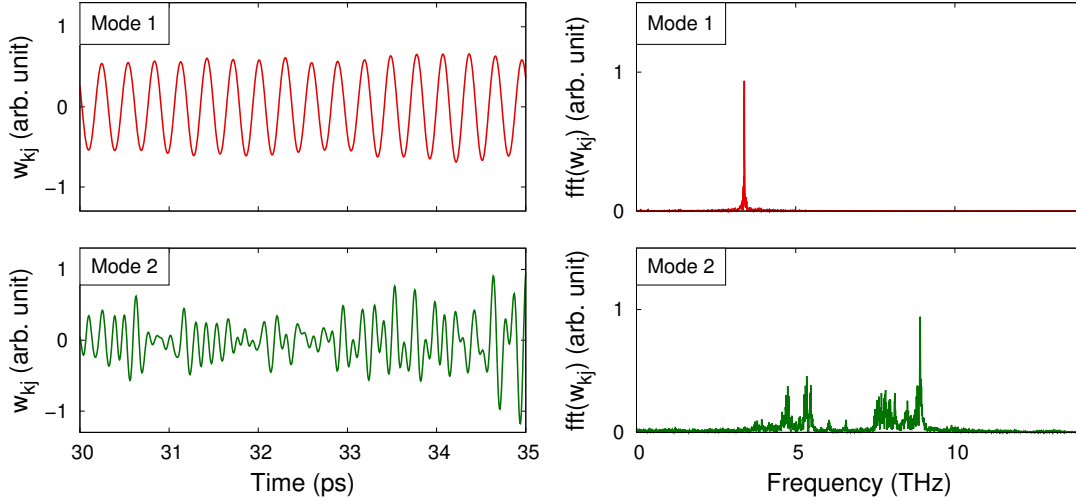


Figure 5.4: The time-evolution of w_{kj} and the Fourier transformation $\text{fft}(w_{kj})$ for mode 1 and mode 2. Harmonic oscillations for mode 1 as expected. The fourier transform of mode 2 has no distinct peak which is required for the singular value decomposition to work.

5.3.2 Effective harmonic models

Simulations are performed in the NVT ensemble with lattice parameters obtained from previous NPT simulations. Fixed volume ensures well defined equilibrium positions, which is necessary since the EHM is based on fitting displacements from these equilibrium positions. The reduced force constant matrices κ are translated to a full force constant matrix, which in turn is transformed to a set of dynamical matrices. Diagonalization of these gives the phonon dispersion.

Since the phonon spectrum determines the free energies, we commence with a comparison of the phonon dispersions and DOS obtained from QHA at 0 K, and EHMs at 200 K and 800 K presented in Figure 5.5. The phonon dispersions show identical symmetry properties, with softening of high energy phonons at elevated temperatures as the only noticeable difference. Furthermore, the two methods generate indistinguishable phonon dispersions in the low temperature limit, which is not explicitly presented here. This excellent agreement is a first indication for the usefulness of EHMs as well as a verification of the implementation of the force constant fit procedure described in section 3.2.2. Phonon density of states (DOS) obtained from EHM and VAC are presented in Figure 5.6. Identical cut-off frequencies and overall agreement is observed.

Next the target forces at each time step are compared with the corresponding forces predicted by EHMs. This is shown in scatter plots in Figure 5.7 at temper-

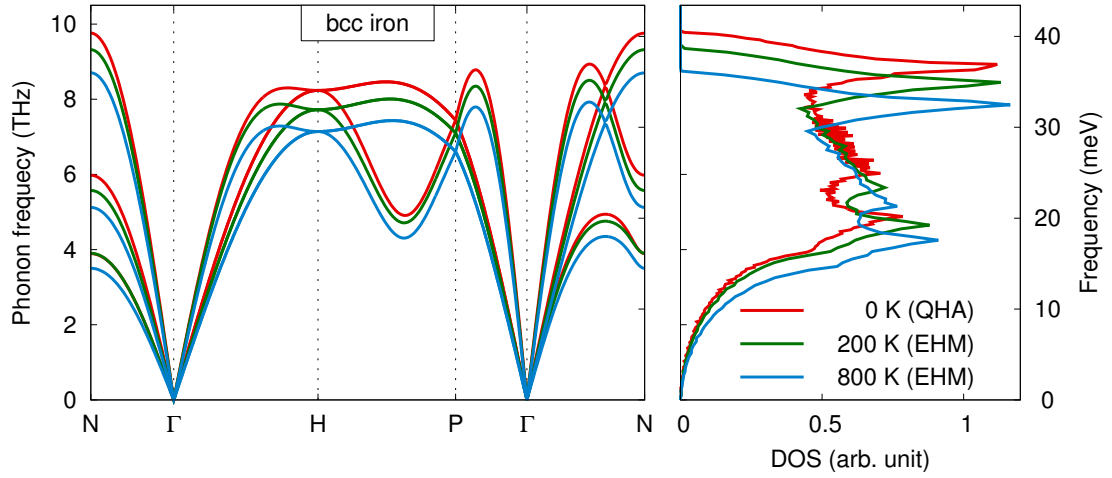


Figure 5.5: Phonon dispersions and density of states (DOS) from QHA at 0 K and EHM at 200 K and 800 K. Softening of high energy modes at elevated temperatures is expected. The methods show excellent agreement as well as identical symmetry properties.

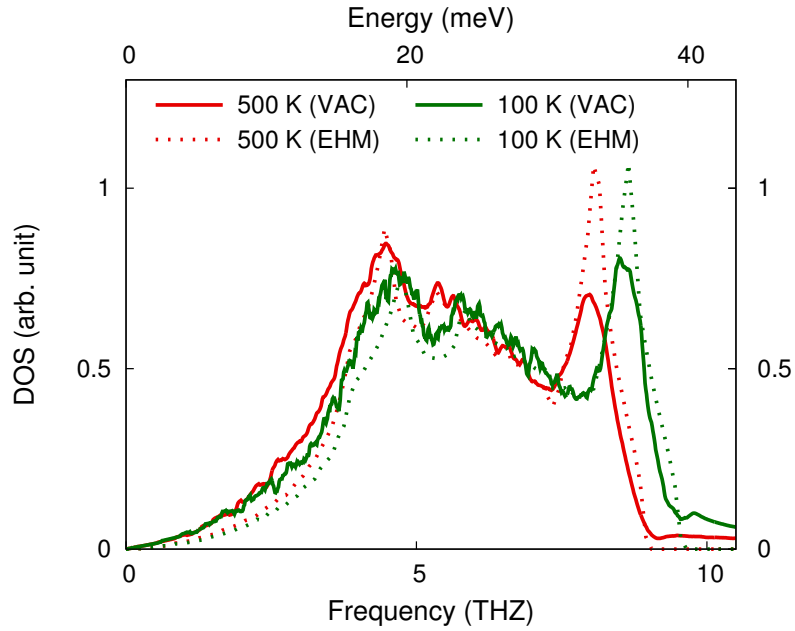


Figure 5.6: Phonon density of states (DOS) obtained from EHM and VAC. Identical cut-off frequencies and overall agreement is observed.

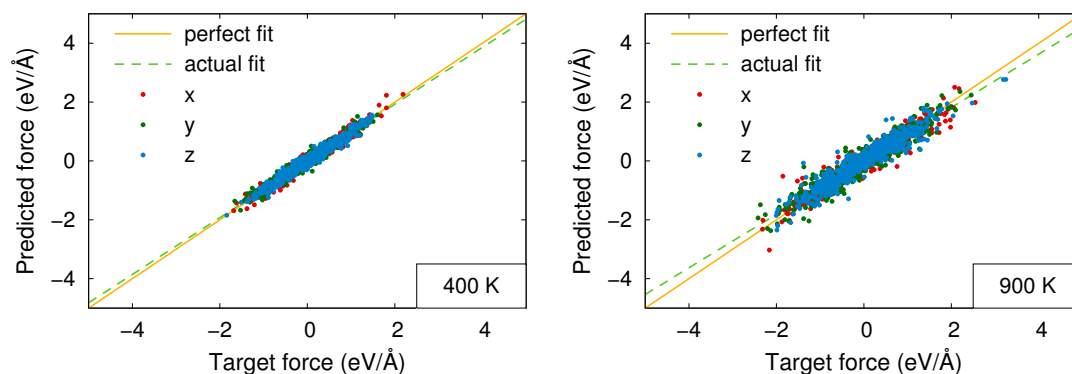


Figure 5.7: These two plots show the goodness of the fit at 400 K and 900 K, to the left and right respectively. The y-axis represents the computed force components. The x-axis represents the target force components. The deviation between a perfect fit and the actual fit is increasing with temperature.

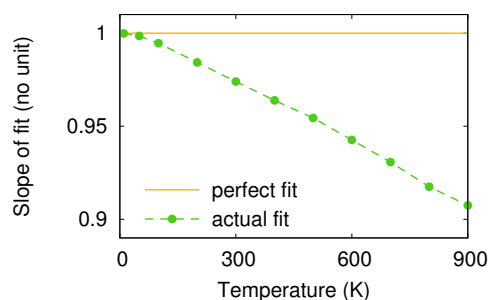


Figure 5.8: The slope of the actual fits obtained from scatter plots as the ones shown in Figure 5.7. For low temperatures the predicted forces from the EHM replicate the target forces very well. For temperatures above 100 K the discrepancy increases approximately linearly.

atures of 400 K and 900 K respectively. For increased temperatures the deviation between a perfect fit and the actual fit increases, see Figure 5.8. Note the excellent agreement in the low temperature limit, where the slope of the fit is one. The slope is monotonically decreasing for increasing temperatures, which is a manifestation of systematic underestimation of the target forces. Again, the key observation is that the discrepancy between the actual fit and a perfect fit is due to bias enforced by the model and not due to statistical uncertainty.

The harmonic free energy deduced from the EHM is presented along with the free energy calculated from the reference method in section 5.4.

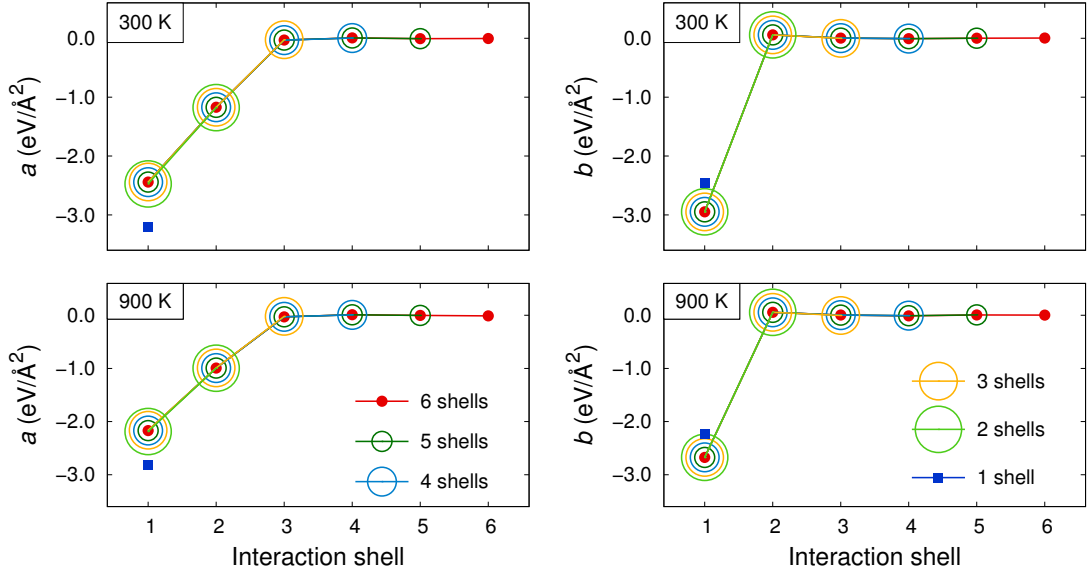


Figure 5.9: Elements of the reduced force constant matrices, where a and b denote diagonal and off-diagonal elements, respectively. The upper and lower panels show data obtained at 400 K and 900 K, respectively. The colors represent the number of neighbor shells that was considered.

Convergence

The number of configurations N_c and the number of neighbor shells N_{nbs} needed to converge the EHM is discussed in this subsection. The convergence has been studied at 300 K and 900 K to quantify the influence of increased thermal energy. In Figure 5.9 the elements of the reduced force constant matrix are plotted. The y-axis specifies the value of the matrix elements, where a are diagonal elements and b are off-diagonal elements. The x-axis specifies the interaction shell, that is nearest neighbor shell ("1"), next nearest neighbor shell ("2"), and so on. The colors indicates the number of neighbor shells included in the fitting. From the panels it seems as if it suffices to include only the 1st and 2nd nearest neighbor shells since the elements in subsequent shells are small in comparison.

Even though the elements in higher neighbor shells are small the impact on the free energy has been analyzed. The free energy was studied as function of N_c and N_{nbs} . It was found that the free energy using $N_{nbs} = 4$ was indistinguishable from the free energy calculated with more neighbor shells taken into consideration. The free energy obtained by using only $N_{nbs} = 2$ or 3 tends to converge to a value that differs slightly from the free energy obtained by using $N_{nbs} = 4, 5$ or 6. This discrepancy is increasing with temperature. For efficiency reasons it is desirable

to use as few neighbor shells as possible and this analysis indicates that $N_{nbs} = 4$ is a reasonable choice.

The number of configurations needed to converge the free energy has been further studied using specifically $N_{nbs} = 4$ and the result is plotted in Figure 5.10. The x-axis represents number of configurations N_c , where the configurations were randomly selected from a 300 ps trajectory. For each N_c the fitting procedure was repeated 50 times with randomly chosen configurations. The standard deviation σ_F of the distribution of free energies is seen to decrease monotonically with N_c . Given a specific convergence criteria the corresponding N_c can be found from this analysis.

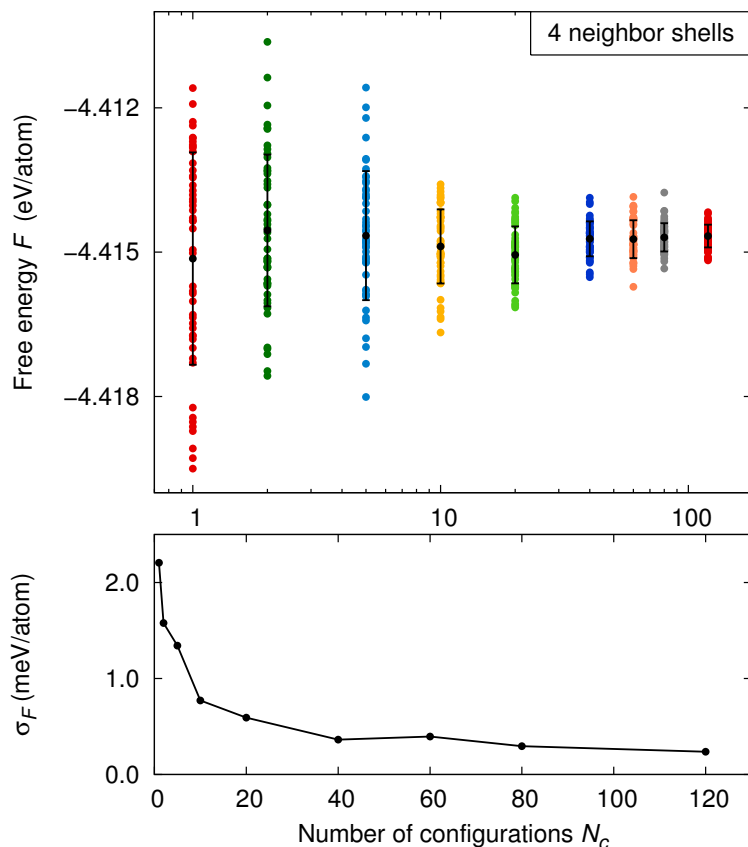


Figure 5.10: Convergence of the free energy with respect to N_c . For each N_c the fitting procedure was repeated 50 times to obtain the statistics presented above. The standard deviation σ_F of the distribution of the free energies for each N_c is indicated by errorbars above and plotted below.

5.4 Method comparison

Figure 5.11 shows a comparison of the free energies from QHA, EHMs and λ -integration. The residual contribution from free energy perturbation (FEP) using Zwanzig's equation is also presented. In the plot below the same quantities are presented with respect to the free energy from λ -integration. The main observations are that the EHM approach is doing significantly better than QHA, and that the EHM are in better agreement with the λ -integration than the EHM with FEP contribution included. This last observation is surprising and a satisfactory explanation has not been found.

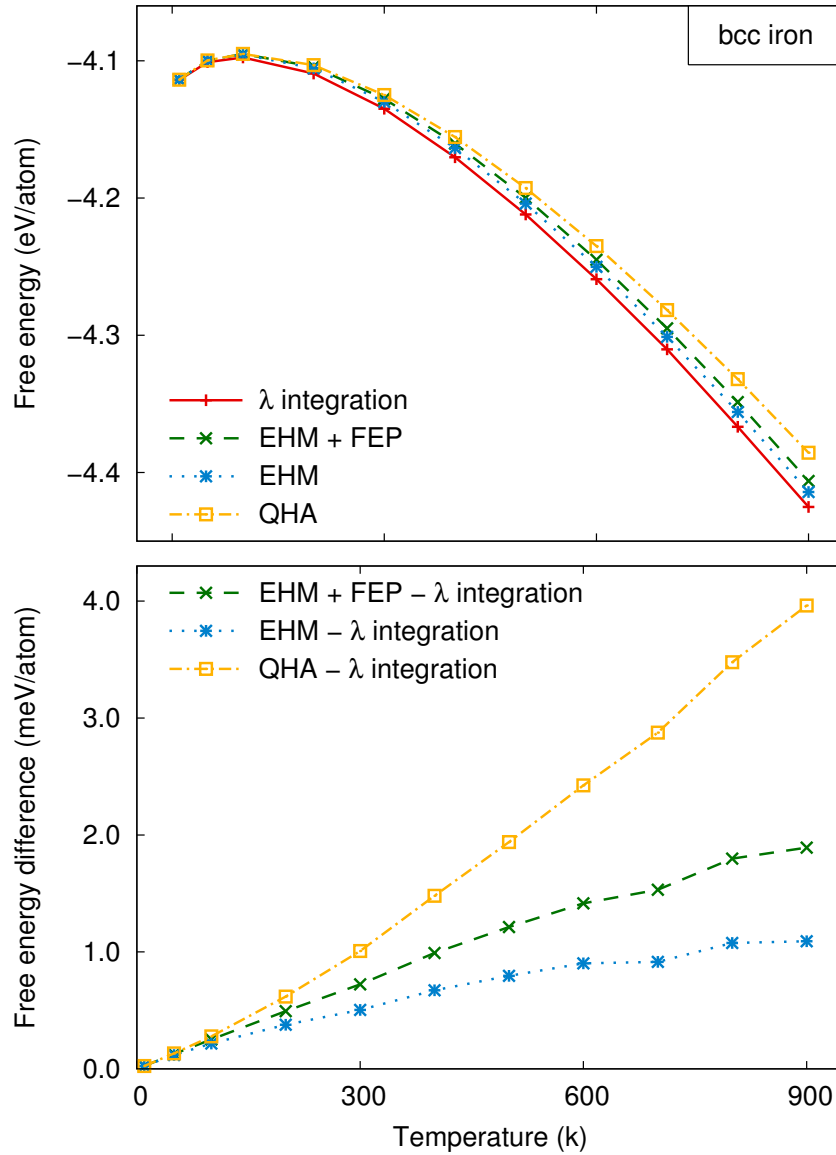


Figure 5.11: Comparison of the computed free energies for bcc iron. Above the free energy from QHA, EHM, λ -integration and EHM with FEP contribution are shown. Below the free energy difference with respect to λ -integration is shown.

6

Titanium

From a structural point of view titanium is non-trivial and displays several phases as function of pressure and temperature [22]. At ambient conditions experiments show stabilization in the hexagonal-close-packed structure (α -phase). For ambient pressure and temperatures above 1200 K it transforms into the body-centered-cubic structure (β -phase). Under pressure the hexagonal (ω -phase) turns out to be most stable. The lattice structures are shown in Figure 6.1. The high temperature β -phase is stabilized by phonon-phonon coupling, and at zero K the phase is mechanically unstable. The QHA, assuming a stable static lattice, is therefore not applicable. In the following it is shown that EHMs, however, do not suffer from this limitation.

The first section 6.1 is presenting estimated transition temperatures from *NPT* simulations in the vicinity of the $\beta \rightarrow \alpha$ transition, where step-like behavior in potential energy is observed for a particular system size. In section 6.2 method details, convergence aspects and results using EHMs, with particular focus on phonon softening and observations of system size effects, are presented. In section 6.3 method analysis and results from λ -integration are presented, for both high temperature $\beta \rightarrow \alpha$ and low temperature $\alpha \rightarrow \omega$ transitions. The chapter is concluded with presenting the calculated phase-diagram, which is based on free energy calculations of α , β and ω -phases.

6.1 Martensitic transition

The $\beta \rightarrow \alpha$ transition has been studied to map out parts of the phase diagram. One of the goals has been to replicate the result presented by Hennig *et al.* in Ref. [22]. For this purpose *NPT* simulations have been performed and the structure as well as

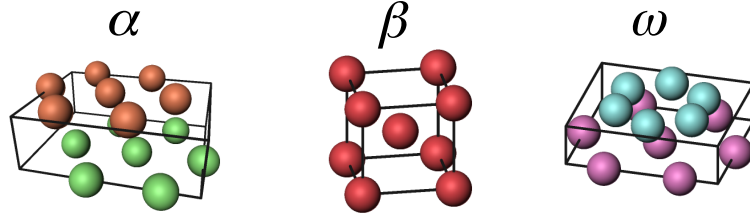


Figure 6.1: The hexagonal-close-packed, body-centered cubic and hexagonal structures α , β and ω , respectively.

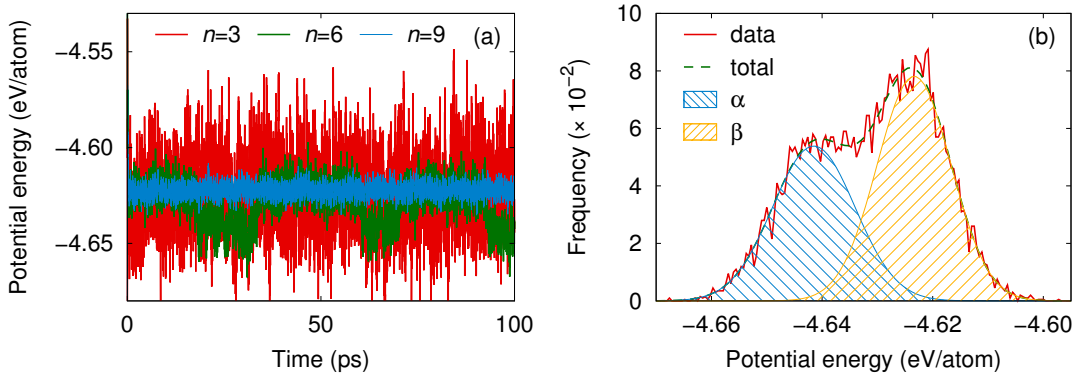


Figure 6.2: (a) Potential energy from *NPT* simulations at 1300 K and 0 GPa for systems sizes $n = 3$ (54 atoms), $n = 6$ (432 atoms) and $n = 9$ (1258 atoms). (b) Double gaussian fit to step-like potential energy for system size $n = 6$.

energy of the system were observed. As temperature is decreased the longitudinal $[110]$ and transversal $\frac{2}{3}[111]$ modes are expected to soften, driving the $\beta \rightarrow \alpha$ and $\beta \rightarrow \omega$ transformations, respectively [10]. The supercell is chosen such that these modes are accessible, which requires cell dimensions, $n_x \times n_y \times n_z$, to be multiples of 3. In Figure 6.2(a) potential energy at 1300 K and 0 GPa from *NPT* simulations is plotted for several system sizes. This particular choice of temperature is expected to be close to the transition temperature at 0 GPa. For the smallest system $n = 3$ (54 atoms) fluctuations in potential energy are large. For the largest system $n = 9$ (1458 atoms) the potential energy is stable exhibiting only modest fluctuations. For the intermediate system size $n = 6$ (432 atoms) potential energy is showing a step-like behavior indicating accessibility of two structures. This dynamics is expected to be observed also for $n = 9$ if the computational time would be extended to increase the number of attempts to overcome the critical nucleation barrier. For $n = 3$ the step-like behavior is dwarfed by large fluctuations.

Assuming the potential energy obeys a Gaussian distribution, the data can be

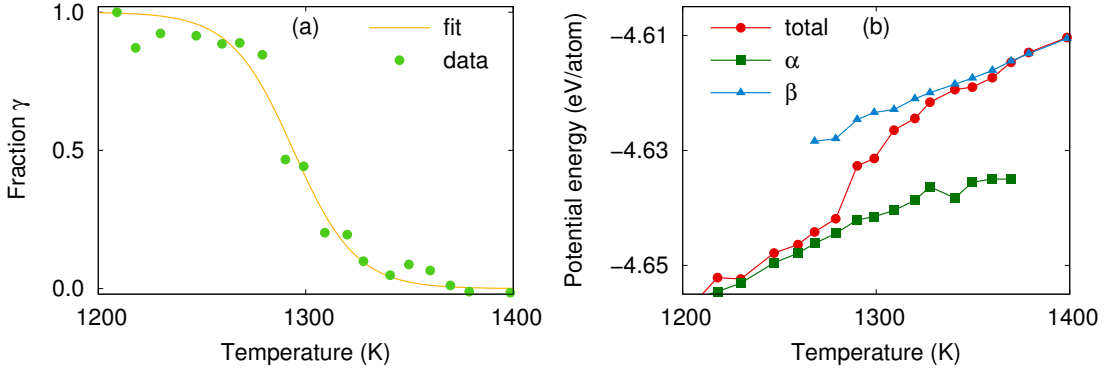


Figure 6.3: (a) Parameter γ defined in eq. (6.1) describing the relative occurrence of α and β -phase. For large values of γ the α -phase is dominating while for small values the β -phase is prevalent. (b) Average potential energy of α and β -phase for different temperatures.

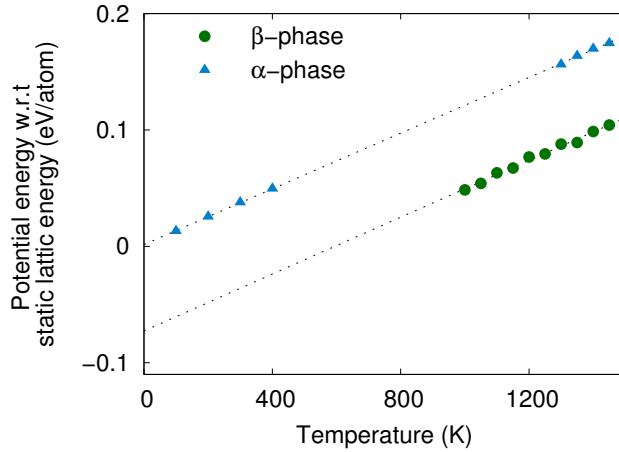


Figure 6.4: Potential energy with respect to the zero K static lattice energy obtained from NVE simulations for α and β -phase. The extrapolated 0 K potential energy is identical zero for the α -phase whereas it is negative for the β -phase, which is a manifestation of the dynamical instability of the β -phase.

fitted to a double Gaussian

$$P(u) = \frac{\gamma}{\sigma_1\sqrt{2\pi}} \exp\left[-\frac{(u - \mu_1)^2}{2\sigma_1^2}\right] + \frac{1 - \gamma}{\sigma_2\sqrt{2\pi}} \exp\left[-\frac{(u - \mu_2)^2}{2\sigma_2^2}\right], \quad (6.1)$$

where u is the potential energy, σ_i , μ_i are the standard deviation and the expectation values for phase i . The parameter γ measures the relative occurrence of β and α -phase respectively. In Figure 6.2(b) the double Gaussian fit to $n = 6$ data at

Table 6.1: Transition temperatures for the $\beta \rightarrow \alpha$ transition, estimated from *NPT* simulations using the double Gaussian ansatz, see eq. (6.1).

Pressure (GPa)	0	2	4	6	8	10	12
Temperature (K)	1294	1278	1279	1249	1330	1380	1410

1300 K is presented. At this particular temperature the β -phase is more prevalent than the α -phase indicating that the transition temperature is slightly below 1300 K.

NPT simulations were performed from 1200 K to 1400 K in increments of 10 K to map out the 0 GPa transition in detail. For each temperature the relative occurrence γ was calculated. The result is presented in Figure 6.3(a) where γ is fitted to a Fermi function

$$\gamma_{fit} = \frac{1}{1 + \exp((T - T_0)/\sigma)}. \quad (6.2)$$

The transition temperature is estimated from the fit as $T_0 = 1294$ K. Furthermore, the potential energies of the α and β -phase as well as the total system are plotted in Figure 6.3(b). In a completely analogous manner, the transition temperature for higher pressures have been determined. In Table 6.1 these transition temperatures are presented.

Up until now observations of the $\beta \rightarrow \alpha$ transition are based on monitoring potential energy in *NPT* simulations. Another approach to study the instability of the β -phase is to fit the forces from *NVT* simulations using EHMs. Since the β -instability is driven by softening of phonons one can expect to see softening in phonon dispersions obtained from EHMs, which is discussed in the next section.

An interesting manifestation of the dynamical instability in the β -phase is seen in the extrapolated 0 K potential energy. The average potential energy was computed from *NVT* simulations in the range 1000 K to 1500 K. In Figure 6.4 the potential energy with respect to the static lattice energy is presented, where the dashed line is a linear fit to the data points. As soon as the temperature is raised above 0 K the β -phase deforms into a structure with lower potential energy and symmetry.

6.2 Effective harmonic models

Simulations are performed in the *NVT* ensemble with lattice parameters obtained from *NPT* simulations. Since the β -instability is driven by phonon softening

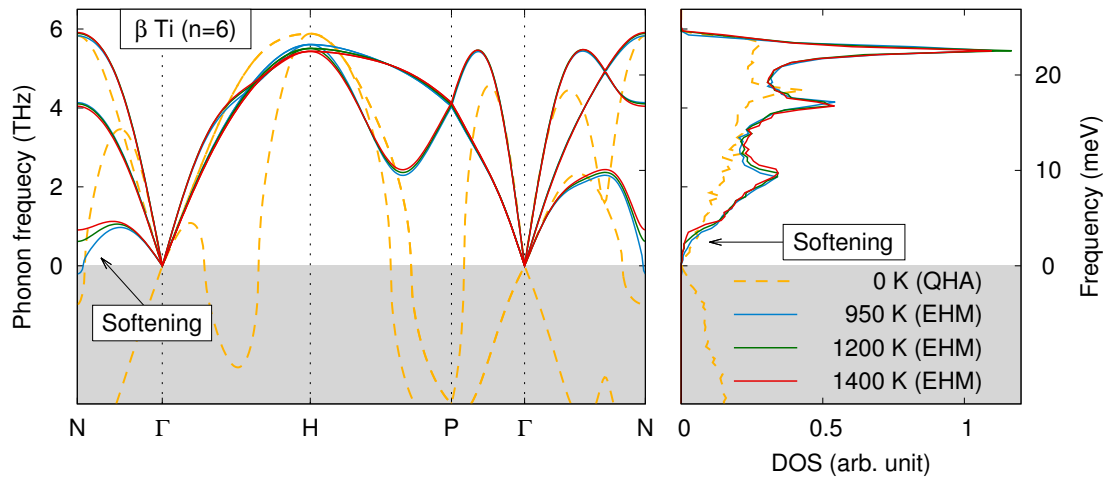


Figure 6.5: Phonon dispersion and density of states (DOS) in β -titanium obtained from EHM at 950 K, 1200 K and 1400 K. Drastic temperature dependence is observed around the N -point where the longitudinal mode is unstable at 950 K. The phonon dispersion at zero K is shown to highlight the inadequacy of the QHA for dynamically unstable systems.

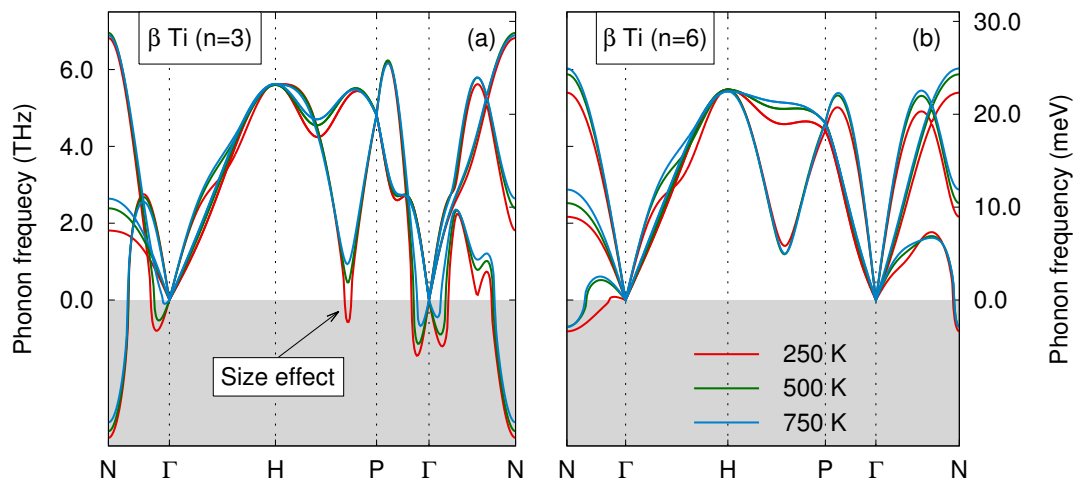


Figure 6.6: Phonon dispersion in β -titanium obtained from EHM at 250 K, 500 K and 750 K. Drastic temperature dependence is observed around the N -point. Even more interesting is the $\beta \rightarrow \omega$ instability along $H - P$, where the softening is pronounced for the smaller system.

one can expect to see softening in phonon dispersions obtained from EHM. The temperature where β goes from being metastable to unstable can then be extracted

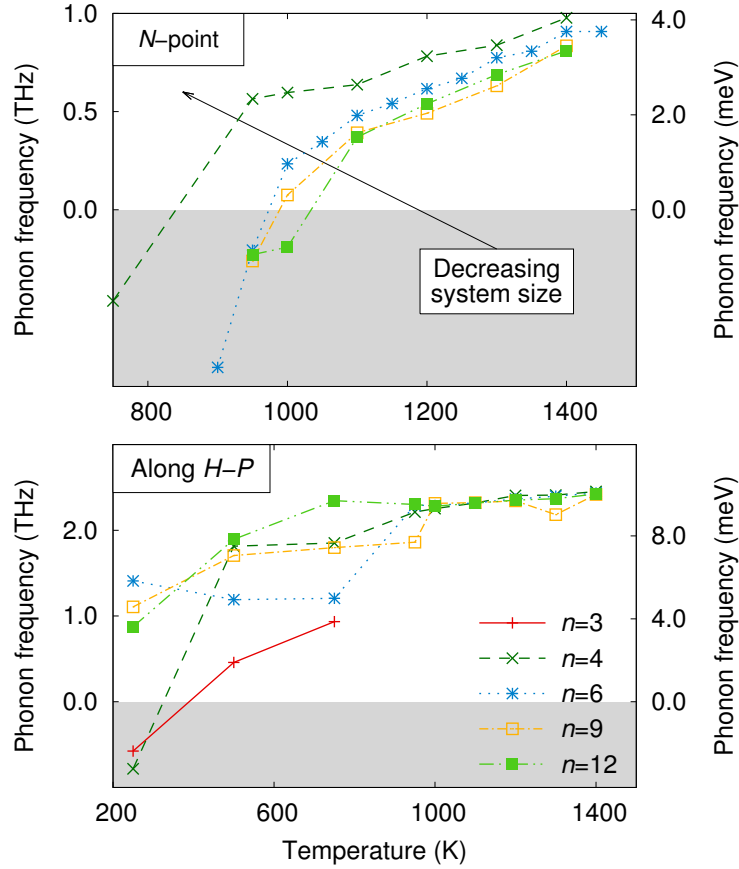


Figure 6.7: Softening at the N -point and along the $H - P$ direction for several systems sizes n .

from the temperature dependence of the respective modes. Phonon dispersions obtained from EHMs at 950 K, 1200 K and 1400 K using system size $n = 6$ are presented in Figure 6.5. At the N -point the most prominent softening is observed, where the longitudinal mode drives the transition. The stabilization temperature is estimated to 975 K from simulations at 50 K increments. The transversal mode along $H - P$ at $2/3[111]$ which corresponds to the $\beta \rightarrow \omega$ instability shows in comparison only modest softening.

Finite size effects for systems with $n = 3, 4, 6, 9, 12$ corresponding to 54, 128, 432, 1458 and 3456 atoms, respectively, has been explored. In Figure 6.6 phonon dispersions from EHMs at 250 K, 500 K and 750 K are presented for $n = 3$ and 6 respectively. The softening along $H - P$ related to the $\beta \rightarrow \omega$ instability is pronounced for $n = 3$, which indicates that small systems can show features not present or as dominating in larger systems. Furthermore, softening around N and along $H - P$ for systems with $n = 3, 4, 6, 9, 12$ is presented in Figure 6.7. At

the N -point, the destabilization temperature converges to a higher temperature for increasing system sizes. Along the $H - P$ direction, only $n = 3$ and 4 are completely destabilized.

6.2.1 Convergence

The number of configurations N_c and the number of neighbor shells N_{nbs} needed to converge the force constant fitting is discussed in this subsection. The convergence has been studied at 1400 K for $n = 6$. In Figure 6.8 converged elements of the reduced force constant matrix are plotted. The y-axis specifies the value of the matrix elements, a are diagonal elements and b are off-diagonal elements. The x-axis refers to the interaction shell, that is nearest neighbor shell ("1"), next nearest neighbor shell ("2"), and so on. The colors represent N_{nbs} which here are shown for $N_{nbs} \leq 6$. The elements of the force constant matrix for titanium are smaller than the ones for iron, which reflects the softer titanium potential.

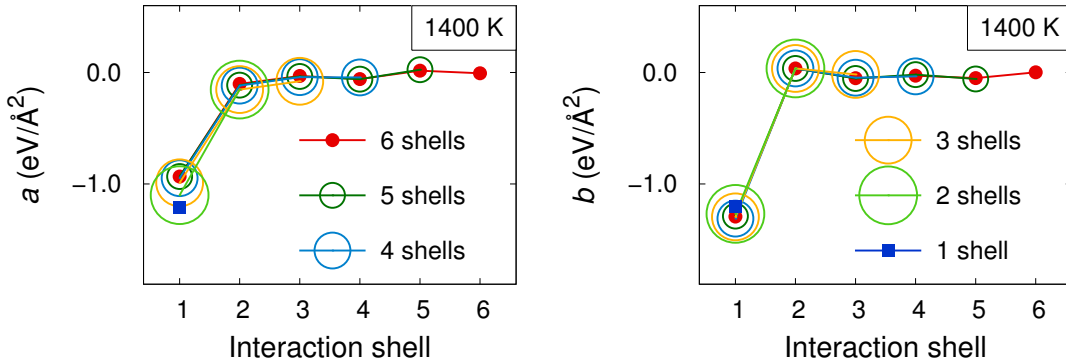


Figure 6.8: Elements of the reduced force constant matrices, where a and b denote diagonal and off-diagonal elements, respectively. The colors represent the number of neighbor shells that was considered.

Even though elements between the 2nd and 6th neighbor shells are small, the impact on the free energy is studied as function of N_c and N_{nbs} . It was found that the free energy using $N_{nbs} = 4$ was in agreement with the free energy calculated using more neighbor shells. The number of configurations needed to converge the free energy has been studied using specifically $N_{nbs} = 4$ and the results are plotted in Figure 6.9. The x-axis represents the number of configurations N_c . The configurations were randomly selected from a trajectory of 300 ps. For each N_c the fitting procedure was repeated 50 times with randomly selected configurations. The standard deviation σ_F of the distribution of free energies is seen to decrease

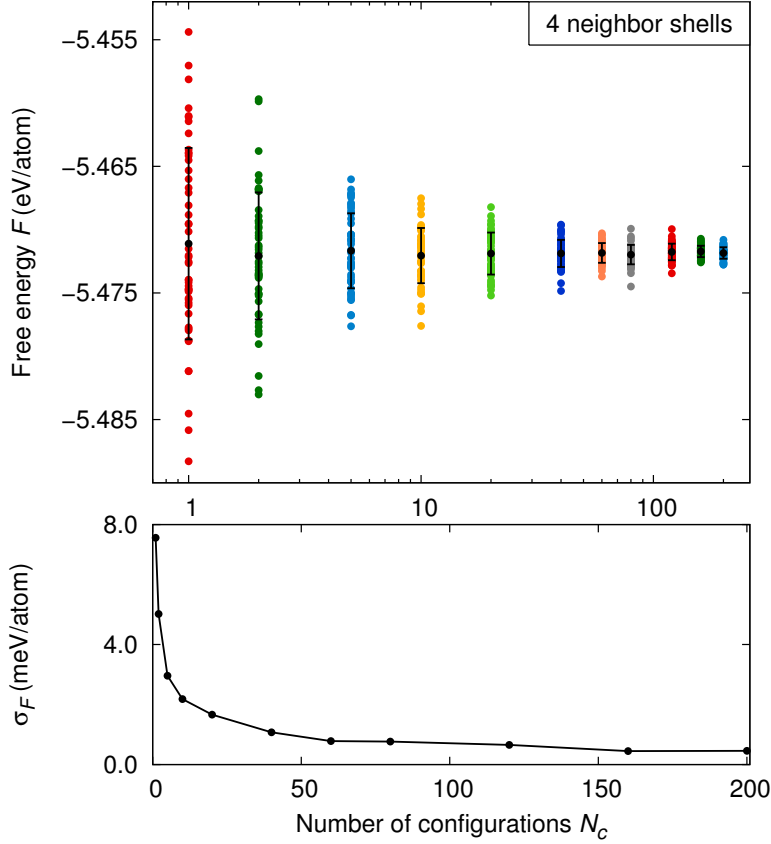


Figure 6.9: Convergence of the free energy with respect to number of configurations N_c . For each N_c the fitting procedure was repeated 50 times to obtain the statistics to in the plot above. The standard deviation σ_F of the distribution of free energies for each N_c is plotted below.

with N_c . Given a specific convergence criteria the corresponding N_c can be found through this analysis.

6.3 λ -integration

Titanium has a complex phase diagram and there are various phase transitions as function of pressure and temperature. To begin with we will revisit the $\beta \rightarrow \alpha$ transition at 0 GPa. From thermodynamics it is well known that minimization of the free energy determines the preferred structure. In Figure 6.10(a) the free energies of α and β -phase at 0 GPa from 1200 K to 1450 K are presented. In this

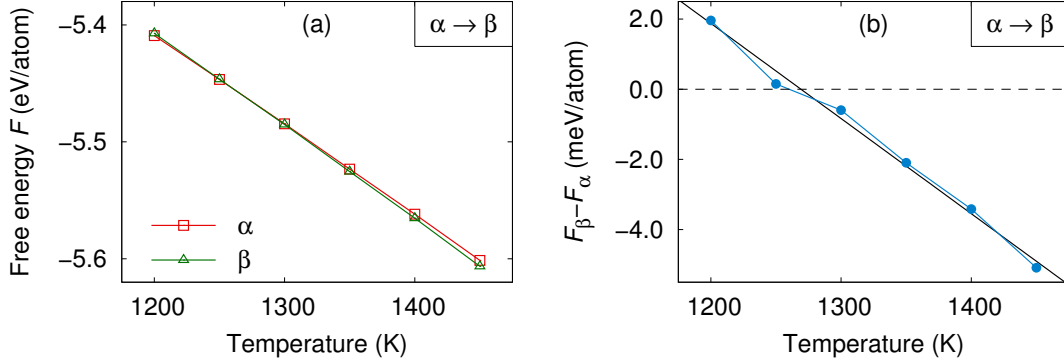


Figure 6.10: Free energies from λ -integration at 0 GPa around the high temperature $\beta \rightarrow \alpha$ transition. In (a) the free energies from the α and β -phase are plotted. It is hard to resolve the transition temperature. In (b) the free energies difference $F_\beta - F_\alpha$ is plotted. The transition temperature is found to be 1270 K.

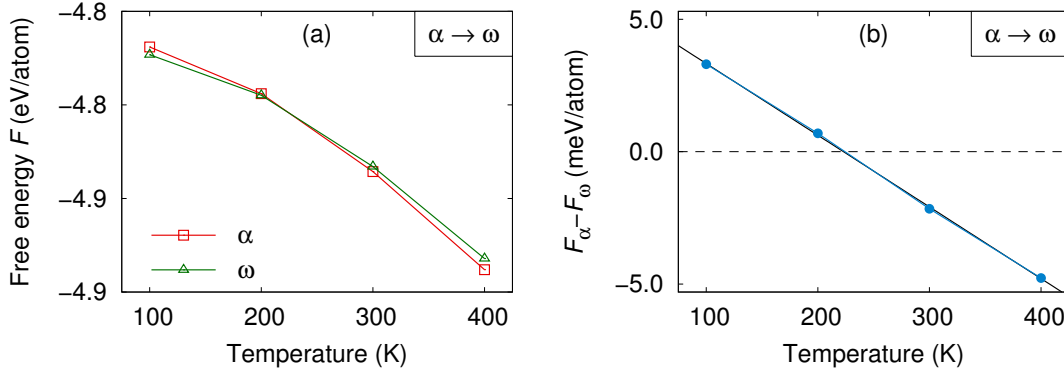


Figure 6.11: Free energies from λ -integration at 0 GPa around the low temperature $\alpha \rightarrow \omega$ transition. In (a) the free energies from the α and ω -phase are plotted. It is hard to resolve the transition temperature. In (b) the free energies difference $F_\alpha - F_\omega$ is plotted. The transition temperature is found to be 223 K.

range both phases exhibit an approximately linear temperature dependence, with a steeper slope for the β -phase. The free energy drops roughly 200 meV/atom for both phases from 1200 K to 1450 K. The free energy difference $F_\beta - F_\alpha$ shown in Figure 6.10(b) is small compared to this drop. The α -phase has lower free energy for positive values and the β -phase has lower free energy for negative values of the difference. The transition temperature is estimated to be 1270 K.

In the range from 1200 K to 1450 K the difference $F_\beta - F_\alpha$ changes by only 7 meV/atom. To ensure reasonable precision in the calculated transition temperature the numerical accuracy and the convergence should be better than 1

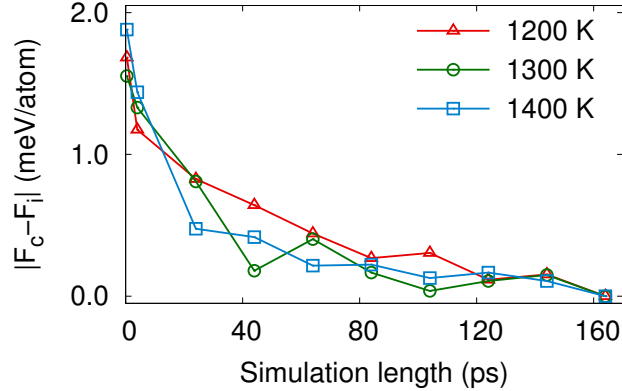


Figure 6.12: Convergence of the free energy difference $|F_c - F_i|$, where F_i is computed from a fraction of the simulation length and F_c is the converged value. The uncertainty in the converged value is smaller than 0.5 meV/atom.

meV/atom. The convergence of $|F_c - F_i|$ is plotted in Figure 6.12, where F_i is computed from a fraction of the simulation length and F_c is the converged value. The uncertainty in the converged value is smaller than 0.5 meV/atom, which gives an estimated uncertainty in transition temperature of ± 20 K.

The $\alpha \rightarrow \omega$ transition has been studied at 0 GPa in the same way as the $\beta \rightarrow \alpha$ transition, where the latter occurs around 1280 K and the previous is expected to occur below 300 K. The free energies for α and ω -phase are presented in Figure 6.11(a) and the difference $F_\alpha - F_\omega$ is shown in 6.11(b). The corresponding transition temperature is found to be 223 K. Furthermore, both $\alpha \rightarrow \omega$ and $\beta \rightarrow \alpha$ transitions have been studied up to 12 GPa. The phase diagram resulting from these free energy calculations will be discussed in section 6.5.

6.4 Method comparison

Figure 6.13 shows a comparison of free energies from EHM and λ -integration. The residual contribution from free energy perturbation (FEP) using Zwanzig's equation is also presented. In the bottom panel of Figure 6.13 the same quantities are presented with respect to the free energy from λ -integration. The main observation is that the FEP contribution significantly improves the raw EHM results with respect to the reference method. In chapter 5 where iron was discussed the free energy from QHA was also presented. It should be recalled that such a comparison is not sensible for β titanium since QHA assumes mechanically stable zero K lattice.

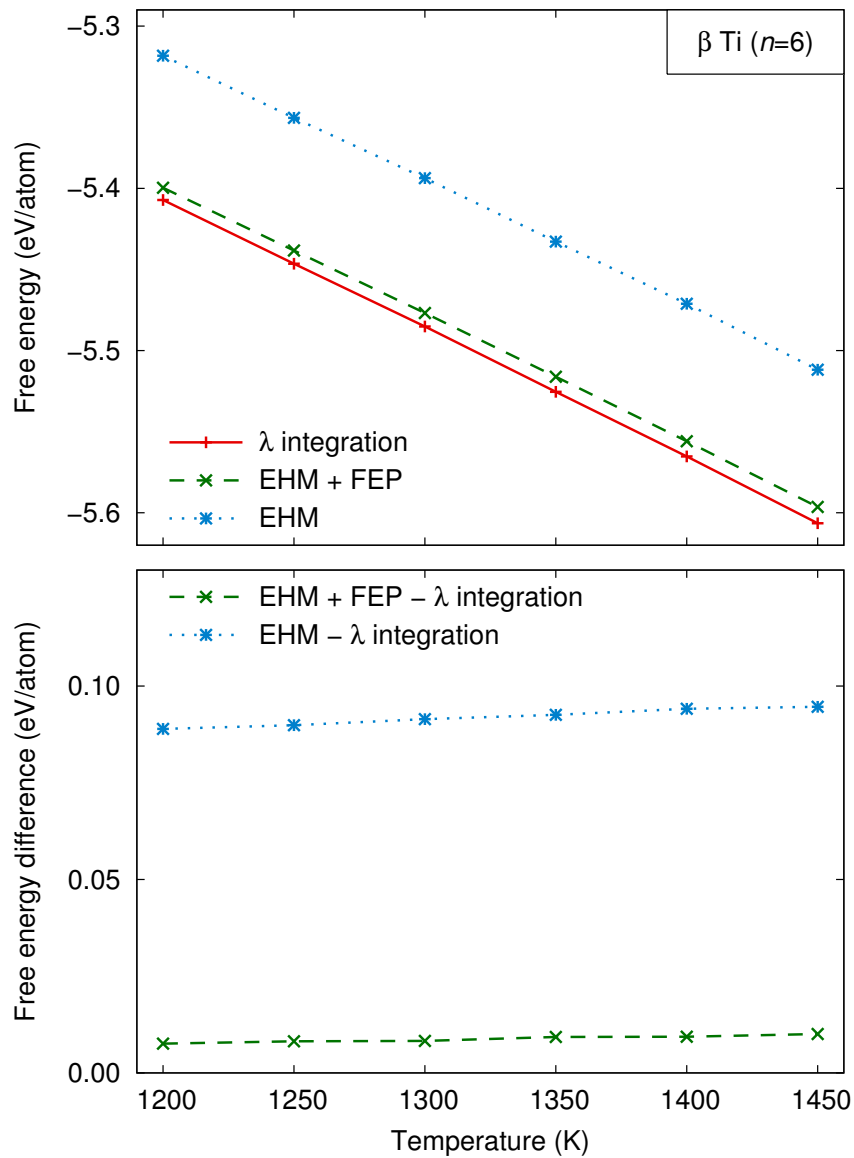


Figure 6.13: Comparison of the computed free energies for β -titanium. Above the free energy from λ -integration, EHM and EHM with FEP contribution are shown. Below free energy differences with respect to the λ -integration are shown.

6.5 Phase diagram

The stability regions deduced from free energy calculations have been compiled into the phase diagram shown in Figure 6.14. Below melting, for temperatures above 1300K and pressures below 10 GPa the β -phase is found to be most stable.

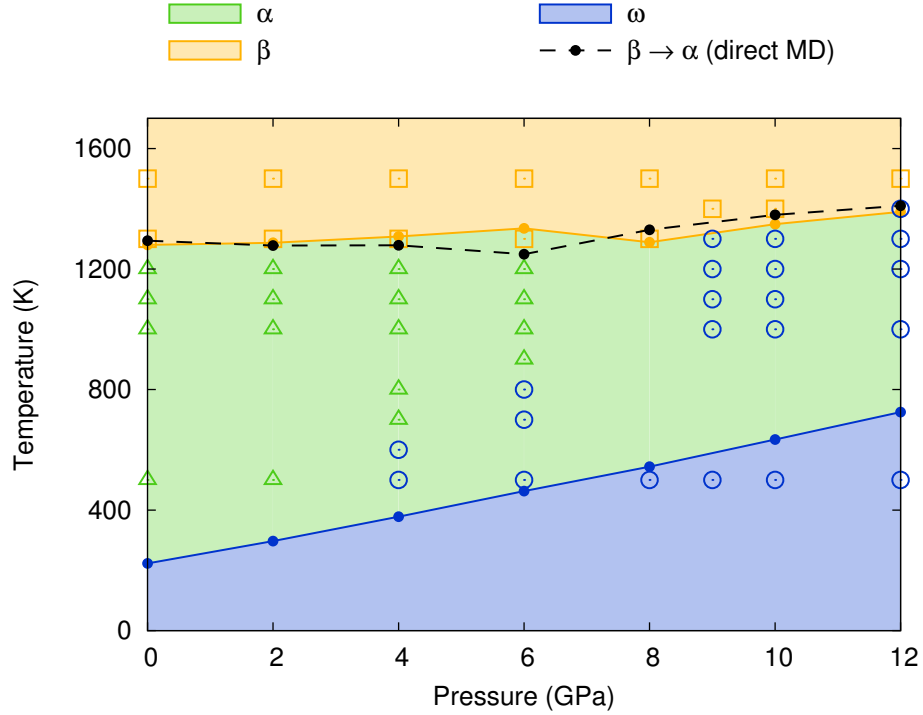


Figure 6.14: Phase diagram for titanium. The background color represents the most stable structure obtain from free energy calculations using λ -integration. The dashed line shows the $\beta \rightarrow \alpha$ transition temperature obtained from studying the instability of the β -phase in *NPT*. The open triangles, circles and boxes represents the equilibrium structure from *NPT* simulations presented in Ref. [22].

Above 10 GPa the $\alpha \rightarrow \beta$ transition temperature increases with pressure.

The $\alpha \rightarrow \omega$ transition temperature increases roughly linear with pressure over the entire range explored in the present work. Experiments show that the α -phase is the most stable structure at ambient conditions, whereas DFT calculations predict the ω -phase to be the most stable at zero temperature and pressure. Since the empirical potential employed in this work has been fitted explicitly to DFT data it reproduced the latter behavior. The free energy calculations locate the $\alpha \rightarrow \omega$ transition, at 0 GPa, at 223 K, which is in good agreement with Ref. [22].

The obtained transition temperatures, from direct MD in section 6.1, for the $\beta \rightarrow \alpha$ transition are also presented in the phase diagram. These temperatures are in good agreement with the free energy calculations in this work as well as the result reported in Ref. [22]. The most notable discrepancy is around 6 GPa where free energy calculations predict a higher transition temperature. As reported in Ref. [22] the transitions in these region exhibit pronounced hysteresis, which implies that free energy calculations should be the most reliable estimator for the

preferred structure.

Monitoring the transition between β and α -phase from observation of the potential energy in the NPT ensemble is enabled by the short time scale of the transformation due to the nature of the transition, and the sampled configuration space which is related to specific simulation settings. The transition is martensitic which are displacive in contrast to e.g. diffusive transitions. Dynamics of displacive transitions is fast compared to very slow diffusive motion hardly observable in simulations. Furthermore, the coupling strength of the thermostat and barostat determines the time scale of changes in temperature and volume, where the $\beta \rightarrow \alpha$ transition requires rapid distortions of the simulation box. The interplay between free energy landscape and sampled configuration space is balanced by the magnitude of fluctuations. Temperature and system size influence the magnitude of fluctuations, and are therefore important parameters.

7

Discussion

The discussion is organized in three sections which reflects the structure of the thesis. First the dimer, then the iron and finally the titanium system are discussed. The ordering of the chapters emphasizes the increasing complexity as one moves from the simple dimer via the stable iron crystal to the full titanium system with the dynamically stabilized β -phase.

7.1 Dimer

The aim with studying the dimer was to apply EHMs to a simple system as well as illustrate general features of harmonic representations. In the language of EHMs the dimer is characterized by a single force constant which is fitted to forces from MD simulations to obtain an optimal harmonic representation. Good agreement between EHMs and the full potential in particular for low velocities is found (Figure 4.1). Increasing velocity leads to an increasing deviation due to the asymmetry of the full potential, which results in underestimated and overestimated forces at small and large bond lengths, respectively (Figure 4.3). From comparison of target forces and predicted forces the small deviation is concluded to be systematic, and hence leading to a bias.

The oscillation frequencies deduced from the EHMs follow the reference frequencies rather well, where the deviation is smaller than 20% even for the largest velocities (Figure 4.2). Within a raw HA, neglecting thermal motion, the oscillation frequency is velocity independent which results in a significantly larger deviation that grows fast with increased velocity.

Even though the dimer is a simplified model system the understanding gained from the study in particular regarding possible sources of bias is helpful when

considering the more complex systems.

7.2 Iron

The motivation for studying the iron system, which is stable from zero K up to the melting point, was to verify and benchmark EHMs *vs.* λ -integration. This has been conducted by comparing phonon DOS obtained from EHMs and VAC, and free energies from EHMs, QHA and λ -integration. Proceeding from the dimer to a many-body system also enabled verification of the symmetrization procedure in the implementation of the EHMs.

λ -integration, used as reference for free energy calculations, works very well for iron. The free energy converges fast with respect to simulation time. Within $t_\lambda = 2$ ps the uncertainty is smaller than 1 meV/atom. Using the entire 180 ps MD trajectory reduces the uncertainty to less than 0.1 meV/atom. This high accuracy and the fact that our λ -integrations are free of bias justify that we use free energies from λ -integration as reference values. To achieve this precision 20 values of λ have been used, which corresponds to $\Delta\lambda = 0.05$. For optimized use of computational resources, without losing too much accuracy, the increment can be set to $\Delta\lambda = 0.1$. From this point of view λ -integration is robust and reliable to use for free energy calculations. Nevertheless, the method is associated with high computational cost, and information about phonon dispersions are not provided stressing the need for complementary methods.

The SVD approach to extracting EHMs was appealing since it in principle would give not only effective harmonic representations but also phonon life times. However, the approach was abandoned as it yields frequency spectra without well-defined peaks, and hence the phonon spectrum is not extractable (Figure 5.4). In the harmonic approximation amplitudes of atomic displacements are determined by temperature and phonon frequency (see e.g. Ref. [26]), whereas in the SVD approach the phonon amplitudes a_k enter as additional parameters [see eq. (3.13)]. Due to these additional degrees of freedom the SVD approach yields frequency spectra without well-defined peaks.

In contrast, it has been shown that by fitting forces obtained from MD simulations one can generate EHMs that well reproduce the vibrational properties at the temperature of interest (section 5.3.2). In the zero K limit phonon dispersions for iron obtained from EHMs and QHA are indistinguishable, and as temperature is increased the phonon dispersion from EHMs is softened relative to QHA (Figure 5.5). This demonstrates that EHMs allow to explicitly take anharmonicity, from not only thermal expansion but also thermal motion, into account. This is supported by the comparison of free energies where the EHM results follow the reference data obtained by λ -integration more closely than the QHA does (Figure

5.11). Taking the residual anharmonic correction from Zwanzig’s equation (FEP) into account was expected to give a further improvement. The opposite, however was observed, a behavior that has not been satisfactorily explained yet.

Using the EHM scheme suggested in this work strongly reduces the number of parameters needed since symmetry properties are used directly in the fit. It is shown that 4 neighbor shells are required to properly describe the system (Figure 5.9), and for 250 atoms in bcc configuration this results in only 7 parameters (section 3.2.2). This is compared with the model proposed by Hellman *et al.* in Ref. [5] for which the same system would have on the order of 10^6 parameters.

The number of configurations required to converge the EHMs is $N_c = 10$, which ensures an uncertainty of less than 1 meV/atom (Figure 5.10). By assuming that the decorrelation time in MD is $\Delta t = 0.2$ ps the required simulation time is estimated to $N_c \cdot \Delta t = 2$ ps. The corresponding simulation time to achieve the same accuracy in λ -integration is approximately $1/\Delta\lambda \cdot t_\lambda = 20$ ps. The conclusion is that the EHM is one order of magnitude faster than λ -integration.

7.3 Titanium

From a structural point of view titanium is more complex than iron and displays several phases as function of pressure and temperature. The high temperature β -phase is stabilized by phonon-phonon coupling and mechanically unstable at zero K. The QHA, assuming a stable static lattice, is therefore not applicable to the β -phase [30]. To show that the EHM is applicable to dynamically unstable systems, and in particular, to determine its accuracy in describing vibrational dynamics, has been a focal point in this work.

The high temperature $\beta \rightarrow \alpha$ transition was monitored in the isothermal-isobaric NPT ensemble by observing discontinuities in potential energy. Studying the transformation in this fashion is enabled by rapid dynamics of martensitic phase transitions and specific barostat settings enabling fast distortions of the simulation box. The interplay between free energy landscape and sampled configuration space is balanced by the magnitude of the fluctuations. Temperature and system size influence the magnitude of fluctuations and are therefore important parameters. In particular it was observed that the potential energy in systems with 432 atoms exhibits discontinuities (Figure 6.2). For larger systems and smaller systems, the discontinuities are absent and dwarfed by noise, respectively. Transition temperatures have been estimated by using double Gaussian fits to the potential energies (Figure 6.2 and Table 6.1). These temperatures are in good agreement with the temperatures reported by Hennig *et al.* in Ref. [22].

Looking closer at the structure resulting from monitoring the $\beta \rightarrow \alpha$ transition in the NPT ensemble it is found that the structure is not purely α but rather a mix

of structures. This has been concluded by comparing potential energies, volumes and structural parameters from α , β and ω NPT simulations. In the reference paper the 432 atom β supercell is claimed to be commensurate with both α and ω -phase if properly strained [22]. From the simulations carried out in the context of the present work it is concluded that the simulation cell indeed deforms to pure ω at low temperatures but the $\beta \rightarrow \alpha$ transition invariably led to strongly defected α structures.

λ -integration, used as reference for free energy calculations, works well also for titanium. Compared to iron the free energy converges slower with respect to simulation time. Within $t_\lambda = 30$ ps the uncertainty is smaller than 1 meV/atom. The reason for longer simulation time, where the corresponding time for iron is 2ps, is that the temperature is higher and that the titanium system is not modelled as well by the Einstein crystal.

The instability of the β -phase has been mapped out by fitting EHM to forces from simulations in the canonical NVT ensemble. The focus has been on quantifying finite size effects and temperature dependence. The EHM captures the softening of the phonon modes in the vicinity of the instability very well. In particular the softening at the N -point is found to drive the instability (Figure 6.5). The corresponding temperature where the β -phase goes unstable is estimated to 975 K for the system with 432 atoms. For larger and smaller systems the instability occurs slightly higher and lower in temperature, respectively (Figure 6.7). Furthermore, the instability driving the $\beta \rightarrow \omega$ transition is only observed in the smallest systems, 54 and 128 atoms, respectively. This indicates that small systems with on the order of 100 atoms or less have to be used with caution as one might observe pronounced features that are not present in larger systems due to finite size effects.

The number of configurations needed to converge the EHM is $N_c = 60$, which ensures an uncertainty of less than 1 meV/atom (Figure 6.9). By assuming that the decorrelation time in MD is $\Delta t = 0.2$ ps the required simulation time is estimated to $N_c \cdot \Delta t = 12$ ps. The corresponding simulation time to achieve the same accuracy in λ -integration is approximately $1/\Delta\lambda \cdot t_\lambda = 300$ ps. The conclusion is that in the case of titanium the EHM scheme is more than one order of magnitude faster than λ -integration, which indeed demonstrates the benefit from using the EHM.

EHM is observed to overestimate the reference free energy from λ -integration by 80 meV/atom (Figure 6.13). This overshoot is a result of the β -phase being mechanically unstable at zero K, and can be understood from observing the extracted zero K potential energy in Figure 6.4 and realizing that in any harmonic model the static lattice energy is added *by hand*. However, the FEP contribution significantly improves the estimated free energy with respect to the reference free energy. The full EHM+FEP result is off with roughly 8 meV/atom which indeed

is a remarkable improvement compared to the bare results. Interestingly in the work by Hellman *et al.* in Ref. [5], the residual correction to the harmonic free energy is not mentioned, whereas in this work the correction is found to be crucial.

Symmetry properties of the α and ω -phase have at the time of writing not been implemented in the EHM fitting code. The EHMs based phase diagram is therefore still to be determined. Verification of the latter with respect to the results from λ -integration will be another important test of the EHM approach.

The phase diagram for titanium deduced from the explicit MD study described in section 6.1 and the free energy calculations in section 6.3 shows good agreement with the phase diagram reported in Ref. [22] as well as in Ref. [31–33]. The general features are very similar with $\beta \rightarrow \alpha$ and $\alpha \rightarrow \omega$ transition temperatures at zero GPa in good agreement. In the present work the $\alpha \rightarrow \omega$ transition above zero GPa is found to have a weaker pressure dependence, which implies that the α -phase is the most stable structure in a larger part of the temperature-pressure phase diagram (Figure 6.14).

The zero GPa phase diagram is presented in the bottom panel in Figure 7.1. The region in which the β -phase is metastable, from 975 to 1270 K, is indicated. The free energy landscape is sketched in the top panel.

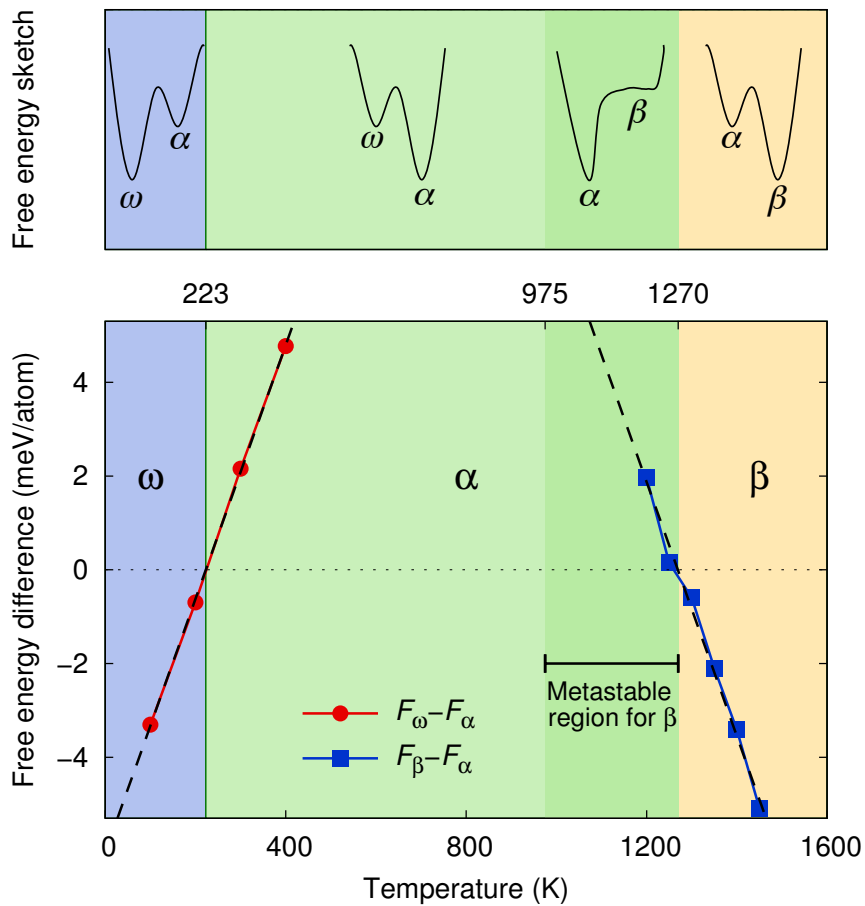


Figure 7.1: Zero GPa phase diagram for titanium obtained from this work. The background colors represent the structure with lowest free energy in respective region. Note that the region where the β -phase is metastable is indicated. The top panel is a sketch of the free energy landscape.

8

Conclusions

The goal of this project has been to develop a computationally efficient method for free energy calculations to enable accurate modeling of a wide range of materials. Using bcc iron as a prototype for a system that is mechanically stable at zero K the accuracy in the computed free energy is concluded to be significantly improved in the EHM approach compared to the QHA. The deviation from λ -integration is 1 meV/atom and 4 meV/atom for EHM and QHA, respectively, implying a relative improvement of 75%. This is an important result for two reasons. Firstly, effectively including anharmonic effects (phonon-phonon coupling) into the model improves the accuracy. Secondly, QHA is inadequate for dynamically unstable materials, thus the EHM presented here is not only more accurate but it can also assess materials where the QHA is inapplicable.

To explore the latter point bcc titanium was considered as a system that is mechanically unstable at zero K and is explicitly stabilized by anharmonic effects. The discrepancy between the EHM free energy and the reference free energy was 80 meV/atom. However, the free energy perturbation contribution from Zwanzig's equation made a significant improvement and reduced the deviation to 8 meV/atom. The relative improvement thus mounts to 90%.

Symmetry was utilized to reduce the number of force constant parameters that had to be fitted. In combination with the fact that the interactions are usually rather short ranged, this implies that for bcc lattices typically only 7 parameters are needed, corresponding to 4 neighbor shells. This number is independent of system size and several order of magnitudes smaller than the corresponding number from the method suggested in Ref. [5].

The EHM is concluded to converge approximately as fast as λ -integration with respect to simulation length. However, the EHM scheme is a one-shot technique whereas λ -integration requires several MD runs, which implies that the new

method is typically at least a factor of ten computationally more efficient. The utility of the approach outlined in this thesis is thus concluded to be highly interesting from the point of view of electronic structure calculations such as DFT.

A flow chart summarizing the connection between simulations and computations utilized in the present thesis is shown in Figure 8.1.

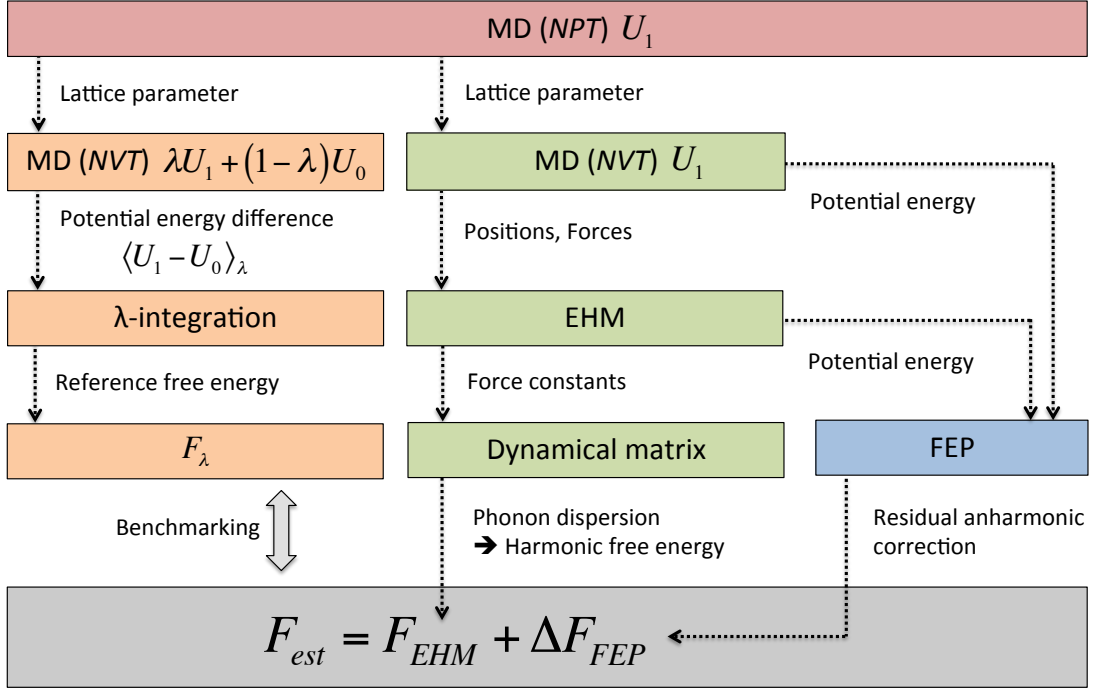


Figure 8.1: Illustration of simulation and computational schemes used in the present work. The lattice parameters (think α , β , ω) for a specific pressure and temperature are obtained from *NPT* MD simulations. The *multi-shot* branch to the left (orange) represents the simulations and computations that are required for λ -integration. The *one-shot* branch in the middle (green) presents the steps in the fitting process where the harmonic free energy is obtained from EHM. In the end the reference free energy is compared with the EHM approach and residual anharmonic correction from FEP.

Bibliography

- [1] Lutjering, G. & Williams, J. C. *Titanium* (Springer, 2010), 2 edn.
- [2] Kohn, W. & Sham, L. J. Self-consistent equations including exchange and correlation effects. *Physical Review B* **140**, A1133–A1138 (1965).
- [3] Souvatzis, P., Eriksson, O., Katsnelson, M. I. & Rudin, S. P. Entropy driven stabilization of energetically unstable crystal structures explained from first principles theory. *Physical Review Letters* **100**, 095901 (2008).
- [4] Souvatzis, P., Eriksson, O., Katsnelson, M. & Rudin, S. The self-consistent ab initio lattice dynamical method. *Computational materials science* **44**, 888–894 (2009).
- [5] Hellman, O., Abrikosov, I. A. & Simak, S. I. Lattice dynamics of anharmonic solids from first principles. *Physical Review B* **84**, 180301 (2011).
- [6] Frenkel, D. & Ladd, A. J. C. New Monte Carlo method to compute the free energy of arbitrary solids. Application to the fcc and hcp phases of hard spheres. *The Journal of Chemical Physics* **81**, 3188–3193 (1984).
- [7] Zwanzig, R. W. High-temperature equation of state by a perturbation method. I. Nonpolar gases. *The Journal of Chemical Physics* **22**, 1420–1426 (1954).
- [8] Tan, T. B., Schultz, A. J. & Kofke, D. A. Suitability of umbrella- and overlap-sampling methods for calculation of solid-phase free energies by molecular simulation. *The Journal of Chemical Physics* **132**, 214103 (2010).
- [9] Petry, W., Heiming, A., Trampenau, J., Alba, M. & Vogl, G. Strong phonon softening in the BCC phase of titanium. *Physica B: Condensed Matter* **156**, 56–58 (1989).

- [10] Petry, W. *et al.* Phonon dispersion of the bcc phase of group-IV metals. I. bcc titanium. *Physical Review B* **43**, 10933 (1991).
- [11] Plimpton, S. Fast parallel algorithms for short-range molecular dynamics. *Journal of Computational Physics* **117**, 1–19 (1995).
- [12] Frenkel, D. & Smit, B. *Understanding molecular simulation: From algorithms to applications* (Academic Press, 2002).
- [13] Parrinello, M. & Rahman, A. Polymorphic transitions in single crystals: A new molecular dynamics method. *Journal of Applied Physics* **52**, 7182–7190 (1981).
- [14] Tuckerman, M. E., Alejandre, J., Lopez-Rendon, R., Jochim, A. L. & Martyna, G. J. A Liouville-operator derived measure-preserving integrator for molecular dynamics simulations in the isothermal-isobaric ensemble. *Journal of Physics A: Mathematical and General* **39**, 5629–5651 (2006).
- [15] Shinoda, W., Shiga, M. & Mikami, M. Rapid estimation of elastic constants by molecular dynamics simulation under constant stress. *Physical Review B* **69**, 134103 (2004).
- [16] Martyna, G. J., Tobias, D. J. & Klein, M. L. Constant pressure molecular dynamics algorithms. *The Journal of Chemical Physics* **101**, 4177–4189 (1994).
- [17] Mendeleev, M. I. *et al.* Development of new interatomic potentials appropriate for crystalline and liquid iron. *Philosophical Magazine* **83**, 3977–3994 (2003).
- [18] Daw, M. S. & Baskes, M. I. Semiempirical, quantum mechanical calculation of hydrogen embrittlement in metals. *Physical Review Letters* **50**, 1285–1288 (1983).
- [19] Daw, M. S. & Baskes, M. I. Embedded-atom method: Derivation and application to impurities, surfaces, and other defects in metals. *Physical Review B* **29**, 6443–6453 (1984).
- [20] Foiles, S. M., Baskes, M. I. & Daw, M. S. Embedded-atom-method functions for the fcc metals Cu, Ag, Au, Ni, Pd, Pt, and their alloys. *Physical Review B* **33**, 7983–7991 (1986).
- [21] Baskes, M. I. Modified embedded-atom potentials for cubic materials and impurities. *Physical Review B* **46**, 2727–2742 (1992).

- [22] Hennig, R. G., Lenosky, T. J., Trinkle, D. R., Rudin, S. P. & Wilkins, J. W. Classical potential describes martensitic phase transformations between the α , β and ω titanium phases. *Physical Review B* **78**, 054121 (2008).
- [23] Kirkwood, J. G. Statistical mechanics of fluid mixtures. *The Journal of Chemical Physics* **3**, 300–313 (1935).
- [24] Müller, M., Erhart, P. & Albe, K. Analytic bond-order potential for bcc and fcc iron-comparison with established embedded-atom method potentials. *Journal of Physics: Condensed Matter* **19**, 326220 (2007).
- [25] Ashcroft, N. W. & Mermin, N. D. *Solid State Physics* (Brooks Cole, 1976), 1st edn.
- [26] Grimvall, G. *Thermophysical Properties of Materials* (North Holland, 1999), 1st edn.
- [27] Born, M. & Huang, K. *Dynamical Theory of Crystal Lattices* (Oxford University Press, USA, 1998).
- [28] Dickey, J. M. & Paskin, A. Computer simulation of the lattice dynamics of solids. *Physical Review* **188**, 1407–1418 (1969).
- [29] Wang, C. Z., Fasolino, A. & Tosatti, E. Molecular-dynamics theory of the temperature-dependent surface phonons of W(001). *Physical Review B* **37**, 2116–2122 (1988).
- [30] Hu, C. *et al.* Theoretical investigation of the high pressure structure, lattice dynamics, phase transition, and thermal equation of state of titanium metal. *Journal of Applied Physics* **107**, 093509 (2010).
- [31] Mei, Z., Shang, S., Wang, Y. & Liu, Z. Density-functional study of the thermodynamic properties and the pressure-temperature phase diagram of Ti. *Physical Review B* **80**, 104116 (2009).
- [32] Young, D. A. *Phase Diagrams of the Elements* (University of California Press, 1991).
- [33] Zhang, J. *et al.* Experimental constraints on the phase diagram of titanium metal. *Journal of Physics and Chemistry of Solids* **69**, 2559 (2008).